



**HAL**  
open science

## Impact of water saturation on seismoelectric transfer functions: a laboratory study of coseismic phenomenon

Clarisse Bordes, P Sénéchal, Julien Barrière, Daniel Brito, Eric Normandin,  
Damien Jougnot

### ► To cite this version:

Clarisse Bordes, P Sénéchal, Julien Barrière, Daniel Brito, Eric Normandin, et al.. Impact of water saturation on seismoelectric transfer functions: a laboratory study of coseismic phenomenon. *Geophysical Journal International*, 2015, pp.1317-1335. 10.1093/gji/ggu464 . hal-01147905

**HAL Id: hal-01147905**

**<https://hal.science/hal-01147905>**

Submitted on 4 May 2015

**HAL** is a multi-disciplinary open access archive for the deposit and dissemination of scientific research documents, whether they are published or not. The documents may come from teaching and research institutions in France or abroad, or from public or private research centers.

L'archive ouverte pluridisciplinaire **HAL**, est destinée au dépôt et à la diffusion de documents scientifiques de niveau recherche, publiés ou non, émanant des établissements d'enseignement et de recherche français ou étrangers, des laboratoires publics ou privés.

Copyright

# **Impact of water saturation on seismoelectric transfer functions: a laboratory study of co-seismic phenomenon**

C. Bordes<sup>1</sup>, P. Sénéchal<sup>1</sup>, J. Barrière<sup>1,2</sup>, D. Brito<sup>1</sup>, E. Normandin<sup>3</sup> and D. Jougnot<sup>4</sup>

<sup>1</sup> *Lab. des Fluides Complexes et leurs Réservoirs - LFC-R UMR 5150*

*Univ Pau & Pays Adour, CNRS, TOTAL, BP 1155 - PAU, F-64013, France*

<sup>2</sup> *European Center for Geodynamics and Seismology, Rue Josy Welter 19, L-7256 Walferdange, Luxembourg*

<sup>3</sup> *Univ Pau & Pays Adour, Innov Adour, PAU, F-64013, France*

<sup>4</sup> *Applied and Environmental Geophysics Group, Institute of Earth Sciences, University of Lausanne, CH1015, Switzerland*

28 April 2015

## **SUMMARY**

Seismic waves propagating in a porous medium, under favorable conditions, generate measurable electromagnetic fields due to electrokinetic effects. It has been proposed, following experimental and numerical studies, that these so-called “seismoelectromagnetic” couplings depend on pore fluid properties. The theoretical frame describing these phenomena are based on the original Biot’s theory, assuming that pores are fluid-filled. We study here the impact of a partially saturated medium on amplitudes of those seismoelectric couplings by comparing experimental data to an effective fluid model. We have built a 1 m-length-scale experiment designed for imbibition and drainage of an homogeneous silica sand; the experimental set-up includes a seismic source, accelerometers, electric dipoles and capacitance probes in order to monitor seismic and seismoelectric fields during water saturation. Apparent velocities and frequency spectra (in the kiloHertz range) are derived from seismic and electrical measurements during experiments in varying saturation conditions. Amplitudes of seismic and seismoelectric waves

and their ratios (*i.e.* transfer functions) are discussed using a spectral analysis performed by Continuous Wavelet Transform (CWT). The experiments reveal that amplitude ratios of seismic to co-seismic electric signals remain rather constant as a function of the water saturation in the  $S_w = [0.2 - 0.9]$  range, consistently with theoretically predicted transfer functions.

**Key words:** Seismoelectric effect, water saturation, porous media, monitoring

## 1 INTRODUCTION

Relative fluid-solid motions induced at the microscopic scale by a seismic wave propagating in porous media generate conversions from mechanical to electromagnetic energy. This transient electrokinetic phenomenon, that can be observed at the macroscopic scale, was first theoretically described by Frenkel (1944). More recently, in a reference paper, Pride (1994) developed the all set of governing equations for the seismoelectric phenomenon in a saturated medium. These equations are based upon the Biot's theory for seismic propagation in porous medium (Biot 1956a,b) and Maxwell's equations for electromagnetism using a volume averaging approach. Pride's complete seismoelectric analytical formulation has been largely used in recent years in numerical computations (Garambois & Dietrich 2002; Guan & Hu 2008; Zyserman et al. 2010; Santos et al. 2011; Zyserman et al. 2012; Warden et al. 2013) in order to discuss potential applications of seismoelectrics as a new geophysical probing method. By deriving the dispersion relations in terms of effective densities, Schakel & Smeulders (2010) proposed an alternative approach, while confirming its consistency with the original Pride's equations. *In the last decade, seismoelectric phenomena were also discussed by considering electrokinetic couplings as a function of the charge density (e.g. Revil & Jardani 2010; Revil & Mahardika 2013; Jougnot et al. 2013; Revil et al. 2014).*

Seismoelectromagnetic measurements are dominated by coseismic responses that accompanies both body and surface waves, but they also may contain signals originating from seismoelectromagnetic radiating waves generated at interfaces. *It is commonly advanced that the analysis of these interfacial seismoelectromagnetic measurements may lead to informations on petrophysical properties of very thin layers (i.e. thinner than a quarter seismic wavelength).* Some encouraging field measurements showed this effect to be measurable, at least for shallow interfaces (Garambois

& Dietrich 2001; Strahser et al. 2007; Haines et al. 2007a,b; Dupuis et al. 2007) and at the ice-bed interface (Kulesa et al. 2006). *However “deeper” studies (Thompson & Gist 1993) are very rare, in particular because the interface radiation is very low in amplitude (Dupuis & Butler 2006), despite significant improvements in signal processing (Butler & Russell 1993; Dupuis et al. 2009; Warden et al. 2012).*

In the last decade, laboratory experiments performed under controlled conditions have provided several datasets on seismoelectromagnetic coseismic and interfacial signals. For example, evidences of coseismic seismomagnetic fields were shown for Stoneley (Zhu & Toksöz 2005) and body waves (Bordes et al. 2006, 2008). By using an apparatus designed for the characterization of fluid dispersion, Dukhin et al. (2010) also performed seismoelectric measurements showing that the magnitude of seismoelectromagnetic current depends on the porosity, pore sizes, zeta potential and elastic properties of the porous matrix. Other studies confirmed that the rocks petrophysical parameters (Zhu et al. 2000; Zhu & Toksöz 2003) and the fluid properties (Chen & Mu 2005; Block & Harris 2006) have strong effects both on the shape and on the amplitude of interfacial radiations. Schakel et al. (2011a,b) eventually showed that laboratory data and numerical predictions were in good agreement in terms of travel times, waveforms and polarity.

Although the dependence of seismoelectromagnetic signals on fluid parameters such as the pore fluid conductivity, pH or viscosity have already been numerically and/or experimentally addressed, the impact of partial saturation has been rarely studied. However, saturation is often not achieved in reservoirs, since those generally contain at least a few percents of gas or oil, strongly influencing mechanical (Bachrach & Nur 1998; Bachrach et al. 1998; Rubino & Holliger 2012) and electric properties of the rock (Archie 1942). Strahser et al. (2011) measured both seismoelectric coupling and electric impedance between electrodes and suggested that the water content should modify seismoelectromagnetic couplings. To our knowledge, the only laboratory experiment was performed by Parkhomenko & Tsze-San (1964) who measured the seismoelectric potential during water imbibition of dried rocks. Their results showed a dependence of the seismoelectric effect on water content, but they did not measure seismic displacements nor acceleration, assuming that it should not vary with a reproducible seismic source. Nevertheless, numerous later

experimental and theoretical studies showed that attenuation of seismic waves depends on the water saturation (Santos et al. 1990; Mavko & Nolen-Hoeksema 1994; Tuncay & Corapcioglu 1996; Carcione 2001; Lo et al. 2005; Masson & Pride 2007; Lebedev et al. 2009; Rubino & Holliger 2012). As a consequence, the dependence of seismoelectric coupling must be addressed in term of transfer function to account for seismic amplitudes variations due to changes in water saturation.

The goal of the present paper is to compare laboratory data with the theoretical predictions from the Pride's theory (1994), extended to partial saturation by an effective fluid model as proposed in Warden et al. (2013). In Part 2, we derive the low frequency and dynamic analytical transfer functions giving the ratio of the local coseismic seismoelectric field to the local acceleration using the Pride & Haartsen (1996) approach. We present in Part 3 the experimental set-up which consists of a 1 m-typical-length-scale container filled with an homogeneous silica sand. Imbibition and drainage were performed in this container while seismic and seismoelectric signals were recorded. A spectral analysis based on a Continuous Wavelet Transform (CWT) presented in Part 4 is then applied to the experimental signals and the results are compared to theoretical predictions. Our conclusion on the impact of saturation on seismoelectric coupling is given in part 5.

## 2 THEORETICAL BACKGROUND

### 2.1 Seismoelectric transfer functions in fluid-filled media

Following Pride's original study (1994), Pride & Haartsen (1996) developed the analytical formulation of the coseismic transfer functions giving the seismoelectric field vector  $\mathbf{E}$  as a function of the grain acceleration associated to compressional P-waves and shear S-waves. By assuming plane waves with an  $e^{-i\omega t}$  dependence in time ( $t$  is time and  $\omega$  is the wave pulsation), the grain acceleration of P and S-waves  $\ddot{\mathbf{U}}_i(\omega)$  can be linked to the displacement  $\mathbf{U}_i(\omega)$  following

$$\mathbf{U}_i(\omega) = -\frac{\ddot{\mathbf{U}}_i(\omega)}{\omega^2} \quad \text{with} \quad i = \text{P, S.} \quad (1)$$

By neglecting the presence of Biot's slow waves, the dynamic coseismic seismoelectric field

can be written as a function of P and S accelerations following :

$$\mathbf{E}(\omega) = \psi_{\text{P-dyn}}(\omega)\ddot{\mathbf{U}}_{\text{P}}(\omega) + \psi_{\text{S-dyn}}(\omega)\ddot{\mathbf{U}}_{\text{S}}(\omega) \quad (2)$$

where  $\psi_{\text{P-dyn}}$  and  $\psi_{\text{S-dyn}}$  are respectively defined as the complex dynamic transfer functions for (fast) P and S-waves defined by:

$$\psi_{\text{P-dyn}}(\omega) = \frac{i}{\omega} \frac{\tilde{\rho}(\omega)L(\omega)}{\tilde{\varepsilon}(\omega)} \frac{Hs_{\text{P}}^2(\omega) - \rho}{Cs_{\text{P}}^2(\omega) - \rho_f} \quad (3)$$

and

$$\psi_{\text{S-dyn}}(\omega) = \frac{i}{\omega} \mu \tilde{\rho}(\omega)L(\omega) \frac{G}{\rho_f} \frac{s_{\text{S}}^2(\omega) - \rho/G}{s_{\text{S}}^2(\omega) - \mu\tilde{\varepsilon}(\omega)}. \quad (4)$$

In equations (3) and (4),  $\mu$  is the magnetic permeability ( $\mu = \mu_0 = 4\pi 10^{-7} \text{V.s.A}^{-1}.\text{m}^{-1}$  in non-metallic rocks),  $\tilde{\rho}$  is the effective density of the fluid in relative motion,  $L$  is the coupling coefficient,  $\tilde{\varepsilon}$  is the effective electrical permittivity of the porous medium,  $\rho$  is the bulk density of the porous medium depending respectively on grain density  $\rho_s$ , fluid density  $\rho_f$  and on porosity  $\phi$ .  $s_{\text{P}}$  and  $s_{\text{S}}$  are respectively the complex slowness of (fast) P and S-waves, and  $H$ ,  $C$  and  $G$  are poroelastic moduli of the medium. The complete set of equations used in the present paper are shown in Appendix A.

By comparing seismic and seismoelectric signals from a field study, Garambois & Dietrich (2001) showed that  $\mathbf{E}(\omega)$  and  $\ddot{\mathbf{U}}(\omega)$  should be proportional at “low” frequencies and for fast P waves. This approximation assumes that electromagnetic fields are in the diffusive regime and that seismic frequencies are much lower than the Biot’s frequency  $f_c$  (Biot 1962) defined by

$$f_c = \frac{\phi\eta_f}{2\pi\gamma_0\rho_fk_0} = \frac{\omega_c}{2\pi}, \quad (5)$$

where  $\eta_f$  is the dynamic viscosity of the fluid,  $k_0$  is the intrinsic permeability of the medium and  $\omega_c$  is the wave pulsation at the Biot’s frequency. The tortuosity  $\gamma_0$  in eq. (5) is estimated here by the relation proposed by Berryman (1981)  $\gamma_0 = (1 - r) \left(1 + \frac{1}{\phi}\right)$  where  $r$  depends on the grain shape ( $0 < r < 1$  for ellipsoidal grains and  $r = 0.5$  for spherical grains).

For frequencies lower than  $f_c$ , Garambois & Dietrich (2001) neglected the dynamic behavior of electrical properties, permeability and electrokinetic coupling. They deduced that the low frequency seismoelectric field  $\mathbf{E}_{\text{P}}$  associated to P-waves is linearly dependent on seismic grain

acceleration and that the low-frequency static transfer function  $\psi_{\text{P-lf}}$  does not depend on the frequency:

$$\mathbf{E}_P(\omega) = \psi_{\text{P-lf}} \ddot{\mathbf{U}}_P(\omega) \text{ for } \omega \ll \omega_c \quad (6)$$

with

$$\psi_{\text{P-lf}} = -\frac{\varepsilon_0 \varepsilon_f \zeta}{\eta_f \sigma_f} \rho_f \left( 1 - \frac{\rho}{\rho_f} \frac{C}{H} \right) = \psi_0 \left( 1 - \frac{\rho}{\rho_f} \frac{C}{H} \right), \quad (7)$$

where  $\zeta$  is the zeta-potential (defined as the static electrical potential at the shear plane when a part of the diffuse layer is transported by fluid flow),  $\varepsilon_0$  and  $\varepsilon_f$  are respectively the vacuum permittivity and fluid's dielectric permittivities ( $\varepsilon_0 = 8.854 \times 10^{-12} \text{F/m}$ ), and  $\sigma_f$  is the electrical fluid conductivity. Garambois & Dietrich (2001) and Strahser et al. (2011) suggested that the terms in parenthesis in eq. (7) could be neglected leading to  $\psi_{\text{P-lf}} \simeq \psi_0$ . We will discuss in the following the degree of validity of the transfer function  $\psi_{\text{P-lf}} = \psi_0$  obtained thanks to this simplification.

Using the same hypotheses as Garambois & Dietrich (2001), we obtain similarly from eq. (4) a low frequency transfer function for shear S-waves

$$\mathbf{E}_S(\omega) = \psi_{\text{S-lf}}(\omega) \ddot{\mathbf{U}}_S(\omega) \text{ for } \omega \ll \omega_c \quad (8)$$

with

$$\psi_{\text{S-lf}}(\omega) = i \frac{\varepsilon_0 \varepsilon_f \zeta}{\eta_f} \frac{\mu}{\omega} \frac{G}{\rho} \rho_f \frac{\phi}{\gamma_0}. \quad (9)$$

We notice in eq. (9) that  $\psi_{\text{S-lf}}$  inversely depends on  $\omega$  whereas  $\psi_{\text{P-lf}}$  is independent of the wave pulsation. Garambois & Dietrich (2001) get a similar result for the formulation of the seismomagnetic transfer function and chose to express the magnetic field versus the grain velocity in order to avoid this frequency dependence.

At this point, it is more convenient to introduce the electrokinetic coupling coefficient

$$C_{ek} = \frac{\varepsilon_0 \varepsilon_f \zeta}{\eta_f \sigma_f} \quad (10)$$

(see Appendix B for a more complete discussion on  $C_{ek}$ ) defined by electrofiltration measurements (Jouniaux & Pozzi 1995; Guichet et al. 2003, 2006). Using  $C_{ek}$  in eqs (2), (7), and (9) eventually

leads to the low frequency expression of the coseismic seismoelectric field:

$$\begin{aligned}
\mathbf{E}(\omega) &= \psi_{\text{P-lf}} \ddot{\mathbf{U}}_{\text{P}}(\omega) + \psi_{\text{S-lf}}(\omega) \ddot{\mathbf{U}}_{\text{S}}(\omega) \\
&= -C_{ek} \rho_f \left[ \left( 1 - \frac{\rho}{\rho_f} \frac{C}{H} \right) \ddot{\mathbf{U}}_{\text{P}}(\omega) - i \frac{\mu}{\omega} \frac{G}{\rho} \frac{\phi}{\gamma_0} \sigma_f \ddot{\mathbf{U}}_{\text{S}}(\omega) \right] \\
&\quad \text{for } \omega \ll \omega_c.
\end{aligned} \tag{11}$$

Using the hypotheses and equations developed in Appendix A as well as the physical values given in Table 1, we have computed the low frequency and dynamic transfer functions in a fluid-filled (saturated) silica sand from eq. (2), (3), (4), (7) and (9). Fig. 1 shows magnitudes and phase angles of the P and S-waves transfer functions. In these fluid-filled sand simulations, which properties were chosen consistently with the experiment presented below, the Biot's frequency is  $f_c = 3570$  Hz.

[Table 1 about here.]

The main information in Fig. 1 is that the predicted  $|\mathbf{E}_{\text{S}}/\ddot{\mathbf{U}}_{\text{S}}|$  ratios are tiny compared to the  $|\mathbf{E}_{\text{P}}/\ddot{\mathbf{U}}_{\text{P}}|$  (factor at most  $10^{-6}$  between those two ratios). Even if the measurements of a seismoelectric field in a transverse direction compared to the main longitudinal P-wave direction may be of interest, the analysis of such small transfer functions in S-waves seems out of reach both numerically and experimentally as already foreseen by Garambois & Dietrich (2001). Note also that as indicated by eq. (11), the coseismic seismoelectric fields associated to P and S-waves are phase shifted by an angle  $\pi/2$  as seen in Fig. 1 b) and d). We conclude that the global ratio  $|\mathbf{E}/\ddot{\mathbf{U}}|$  is useless as soon as P and S-waves coexist in the seismic signal, since only the P-waves are efficiently converted into electric field: the magnitude of the ratio  $|\mathbf{E}/\ddot{\mathbf{U}}|$  is shifted towards smaller values compared to the analytical P transfer function  $\psi_{\text{P-dyn}}$  when S-waves are present.

Computations in Fig. 1 confirm that the low frequency approximations  $\psi_{\text{P-lf}}$  and  $\psi_{\text{S-lf}}$  are consistent with the dynamic transfer functions  $\psi_{\text{P-dyn}}$  and  $\psi_{\text{S-dyn}}$  as long as the current frequency is below the Biot's frequency (Garambois & Dietrich 2001). This behavior is in good agreement with experimental measurements of frequency dependent coupling coefficients (Reppert et al. 2001; Tardif et al. 2011). For  $f \gg f_c$ , the magnitude of the dynamic transfer function for P-waves strongly decreases as the frequency increases. It is also worth to notice in Fig. 1 a) and b) that



although the computation for  $f \ll f_c$  of the simplified low frequency transfer function  $\psi_0$  gives a correct magnitude (within 3 percents) compared to  $\psi_{P-dyn}$  or  $\psi_{P-lf}$  formulations,  $\psi_0$  is phase shifted by  $\pi$  compared to  $\psi_{P-dyn}$  or  $\psi_{P-lf}$ . As a consequence, the seismoelectric signals predicted by the simplified low frequency transfer function  $\psi_0$  have to be used cautiously since it may lead to some misinterpretations regarding the polarity of the seismic signal compared to electrical signal.

[Figure 1 about here.]

## 2.2 The effective fluid model

The theoretical transfer functions shown in Part 2.1 were developed for fluid-filled porous media since they were based on the original Biot's formulation. However, partial saturation has a strong impact on both seismic propagation and electrokinetic coupling. As long as the seismic wavelengths are much larger than the fluid heterogeneities, the simplest way to account for this partial saturation is to use effective fluid models as basically performed in seismic surveys (Bachrach & Nur 1998) or laboratory measurements (Barrière et al. 2012).

For this purpose, the terms  $\rho_f$ ,  $\rho$ ,  $C$ ,  $H$ ,  $\sigma_f$  and  $C_{ek}$  in eq. (3), (4) (dynamic formulation) and (11) (low frequency formulation) are replaced by their effective values depending on the water saturation  $S_w$  (defined as the pore volume ratio filled with water). The details of this classic effective model are given in Appendix A. Several models of electrokinetic coefficient  $C_{ek}(S_w)$  accounting for partial saturation were constructed from theoretical studies and/or laboratory measurements (Guichet et al. 2003; Darnet & Marquis 2004; Revil & Cerepi 2004; Revil et al. 2007; Allègre et al. 2010; Jackson 2010; Allègre et al. 2012). *The Biot frequency  $\omega_c$  is therefore strongly affected via its dependence on  $\rho_f(S_w)$  and  $\eta_f(S_w)$ .* The various  $C_{ek}(S_w)$  models used in the present study are described in Appendix B; all the electrokinetic models can be written under the following expression  $C_{ek}(S_w) = C_{ek}(S_w = 1)f(S_w)$  where  $f(S_w)$  are listed in Table 2 for the different models. The way we have derived the saturated value of  $C_{ek}(S_w = 1)$  is also detailed in Appendix B.

Computations of the  $C_{ek}(S_w)$  models presented in Fig. 2 in the  $S_w = [0.2 - 1]$  range show that, using the parameters of our experiment, two main trends are expected: Guichet et al. (2003) and Revil et al. (2007) models predict an increase of  $C_{ek}(S_w)$  when  $S_w$  increases, whereas Jack-

son (2010) model predicts the opposite behaviour. Indeed, the choice of the electrokinetic model  $C_{ek}(S_w)$  is rather important since  $C_{ek}$  amplitudes can vary by a factor of ten between various models in the considered saturation range.

[Table 2 about here.]

We will discuss in the following the effect of water saturation on seismoelectric transfer functions amplitudes. Since the use of all these models at once would make our discussion more complex, we propose to use the model of Jackson (2010),  $C_{ek}(S_w) = C_{ek}(S_w = 1)S_e S_w^{-n}$ , as a reference, since it predicts values close to the experimental measurements presented in part 4.

[Figure 2 about here.]

### 2.3 Seismoelectric transfer functions in partially saturated sands

We have presented in Part 2.1 both the dynamic and low frequency transfer functions in a fluid-filled silica sand. We have used the effective properties of the fluid and electrokinetic models to rewrite key terms depending on the water saturation in Part 2.2. The physical parameters needed to express the transfer functions as a function of partial saturation are listed in Table 3.

[Table 3 about here.]

Using the hypotheses of the calculation detailed in Appendix A, Fig. 3 presents magnitudes and phase angles of the partial saturation transfer function  $\psi_{P-dyn}(S_w, \omega)$ ,  $\psi_{P-If}(S_w)$ ,  $\psi_0(S_w)$  as a function of the water saturation. We clearly see that the Biot's frequency (white line in Fig. 3 a)), varies significantly in the  $S_w = [0-1]$  range. Fig. 3 a) displays the evolution of the magnitude  $|\psi_{P-dyn}(S_w, \omega)|$  in a colormap representation as a function of the saturation and the frequency: it shows that, using the Pride's theory (1994) extended to effective fluid models with Jackson (2010) model, the magnitude of the dynamic transfer function is expected to remain rather constant in the  $S_w = [0.2 - 0.9]$  saturation range. Note that the choice of the  $C_{ek}(S_w)$  model (among the ones seen in Appendix B and in Table 2) can affect the shape of the magnitude of  $\psi_{P-dyn}(S_w)$  from a clear increase to a rather constant behaviour (*see the solid black, blue and green curves of figure 3 b) respectively obtained by using Jackson (2010), Guichet et al. (2003) and Revil*

*et al.* (2007) ). For very high saturations (close to  $S_w = 1$ ),  $|\psi_{\text{P-dyn}}(S_w, \omega)|$  strongly decreases toward 0 before a final increase to the value of the saturated transfer function described in Part 2.1. This effect is even better seen in Fig. 3 b) and c) which shows the magnitudes and phase angles of the transfer functions  $\psi_{\text{P-dyn}}$ ,  $\psi_{\text{P-lf}}$ ,  $\psi_0$  at a particular frequency  $f = 1.5$  kHz (close to the experimental measurements presented in Part 3). Minimum values of  $|\psi_{\text{P-dyn}}|$  and  $|\psi_{\text{P-lf}}|$  in Fig. 3 b) corresponds to the specific saturation ( $S_w \simeq 0.99$ ) where important changes occur in the transfer function close to  $S_w = 1$ , originating from strong changes in the poroelastic moduli  $K_U$ ,  $H$  and  $C$  (Bachrach & Nur 1998). Since the term involving the poroelastic moduli contribution was neglected in the expression of the simplified low frequency transfer function  $\psi_0$  (see eq. (7)),  $\psi_0(S_w)$  does not quite follow the amplitudes of the complete expression  $\psi_{\text{dyn}}(S_w)$ , leading to the conclusion that  $\psi_0$  should not be used in partially saturated media.

The low frequency transfer function  $\psi_0(S_w)$  is expected to increase rapidly in the  $S_w = [0.2 - 0.3]$  range whereas  $\psi_{\text{dyn}}(S_w)$  increases more gradually. Eventually, dynamical effect at 1.5 kHz are expected to be very strong (*i. e.*  $\psi_{\text{P-dyn}} \gg \psi_0(S_w)$ ) in the  $S_w = [0.3 - 0.8]$  since the considered frequency is higher than the Biot frequency (Fig. 3 a).

In order to summarize Part 2, the computations performed for a silica sand indicate that:

- the predicted  $|\mathbf{E}_i/\ddot{\mathbf{U}}_i|$  ratios are at least  $10^6$  times higher for P-waves than for S-waves. We then conclude with two points: 1) the S-waves being converted very poorly into electric field, it is hopeless both numerically and experimentally to work with an S-wave seismoelectric field; 2) if one wants to use quantitatively the amplitude of transfer P-waves functions  $\psi_{\text{P-dyn}}$ , the seismic signal should be purely composed of P-waves otherwise the measured magnitude  $|\mathbf{E}_P/\ddot{\mathbf{U}}_P|$  would be underestimated;
- using the Jackson (2010) model for electrokinetic coupling, the theoretically predicted  $|\mathbf{E}_P(S_w, \omega)/\ddot{\mathbf{U}}_P(S_w, \omega)|$  does not vary significantly in the saturation range  $S_w = [0.2-0.9]$ ;
- working in the kilohertz range, low frequency approximation may overestimate  $|\mathbf{E}_P/\ddot{\mathbf{U}}_P|$  ratios especially for saturations close to  $S_w = 0.4$ .

[Figure 3 about here.]

In the next part of the paper, we present a laboratory experiment designed to record seismo-electric data during variations of water saturation. The goal of this experiment is to address the question of the validity of the transfer functions by comparing measured  $|E_P/\ddot{U}_P|$  ratio to theoretical predictions.

### 3 EXPERIMENTAL SET-UP

#### 3.1 Description of the experimental set-up

Our experimental apparatus (Barrière et al. 2012) described below was built to measure seismic and coseismic fields for various water content in a very permeable and homogeneous medium. A necessary condition to observe properly the propagation of direct P-waves is to get at least several wavelengths along the sample length. The porous medium is a sand extracted from a sandpit located in the Landes forest (South West of France), composed of 99% of quartz, which main grain size is around  $250 \mu\text{m}$ . The very low seismic velocities in uncompacted sand involve short wavelengths that enable to built reasonably sized experiments (1 m length-scale container).

[Figure 4 about here.]

The final device shown in Fig. 4 was composed of:

- a wood container filled with uncompacted sand (34 cm x 35 cm x 107 cm) which bottom and lateral edges were covered by acoustic foam (Strasonic foam, Paulstra) to attenuate refracted and reflected seismic waves;
- *5 wells consisting of unperforated PVC pipes: imbibition was performed by injecting water under the effect of gravity through the lower extremity of wells marked by blue arrows in Fig. 4) whereas drainage was performed by pumping water through the wells marked with red arrows;*
- an acoustic source (pendulum) consisting in a stainless steel ball hitting a granite cylinder in contact with the sand. An accelerometer placed on the granite cylinder recorded the source signal: the obtained broad-band spectrum lies in the [0.005-20] kHz frequency range (see Fig. 4 b) and c)). This seismic source was designed to generate mainly P-waves along the  $x$ -axis (Sénéchal et al. 2010);

- 9 single component accelerometers (IEPE type, Bruel and Kjaer) with a  $50 \text{ mV/m}\cdot\text{s}^{-2}$  sensitivity in the [0-17] kHz range. The accelerometers were aligned with the axis of the granite cylinder and placed in the same direction to obtain a null angle of incidence for the direct P-waves ( $x$  direction). They were placed every 10 cm, starting from 20 cm to 100 cm from the source. The accelerometers were oriented in order to get a negative polarity first arrival in acceleration  $\ddot{U}$ , corresponding to a positive scalar product between wave vector and local displacement  $U$  (see eq. (1));

- 8 electric dipoles, composed of two stainless steel electrodes (7 cm long) and their home-made pre-amplifiers (input impedance  $1 \text{ G}\Omega$ ) used for the seismoelectric acquisition. The dipole line ( $x$  direction) is in the direction of the accelerometer line but translated by 1 cm laterally (see Fig. 4). The 10 cm-length dipoles were placed every 10 cm from 20 to 90 cm from the source. Since the negative electrode (by convention in our set-up) is located further from the source (the spatial reference) than the positive electrode, the measured difference in electrical potential is  $-\Delta V_x$  and  $\Delta x = 10 \text{ cm}$ . The seismoelectric field is deduced from this measurement by the relation:

$$E_x = -\frac{\Delta V_x}{\Delta x}. \quad (12)$$

- 6 calibrated capacitance probes (Waterscout SM 100 soil moisture sensor from Spectrum technologies) were used to monitor the water saturation  $S_w$  in the plane where accelerometers and dipoles were located. The water saturation uncertainty was evaluated to 5% and the  $S_w$  value around each accelerometer or dipole was obtained by interpolation of probe measurements using the Inverse Distance Weighting method (Barrière et al. 2012). *The uniform saturation along the receivers line is shown in figure 5*);

- dynamic signal acquisition modules PXI-4498 from National Instruments with 16 simultaneous 24-bit analog inputs per module (316 mV full scale for electrical potential measurements). A 200 kHz sampling rate was used.

### 3.2 Description of the experimental constraints and parameters

Before starting an experiment, we took care to bring the saturating fluid at electrochemical equilibrium by flowing deionized water through the sand during 48 hours. The water conductivity reached a plateau value around  $1.17 \times 10^{-2}$  S/m at 25°C, and the monitoring during the following experiments showed it to be very stable. In the present study, we have neglected the surface electrical conductivity (see Appendix A) in particular because it is generally admitted to be lower than  $2 \times 10^{-4}$  S/m for silica as long as the water conductivity remains about  $10^{-2}$  S/m (Glover 1998; Guichet et al. 2003).

The oven-dried sand were poured in the container with constant flow by using a large sieve. At the end of the experiment, 5 cores were extracted from the sample in order to measure their porosity and intrinsic permeability. Permeability was measured by a home made Darcy's apparatus and was estimated to  $k_0 = 1.02 \times 10^{-11}$  m<sup>2</sup>. The porosity  $\phi = 0.4 \pm 0.02$  was measured by comparing the weight of dried cores to the density of solid grains. *Using the Archie's law, we also verified by laboratory measurements that the formation factor  $F = \phi / \gamma_0$  is close to 4.3 consistently with the  $\gamma_0$  value obtained by the formulation of Berryman (1981).*

Injection pressure was obtained by uplifting water containers 40 cm above the tank. Two initial complete cycles were performed to homogenize pore fluid distribution: the first imbibition started from oven-dried sand and was followed by a first drainage and a second complete cycle. During the last cycle, water saturation variations showed that the saturation could be considered as spatially homogeneous in the horizontal plane of measurements (figure 5).

[Figure 5 about here.]

We explored the  $S_w = [0.2-0.9]$  range corresponding to respectively the water and gas residual saturations. We performed a time-lapse monitoring while the saturation was varying, by repeating about 25 times (between  $S_w = 0.2$  and  $S_w = 0.9$ ) a measurement of an initial saturation measurement followed by ten seismic/seismoelectric records and a final measurement of the saturation. For each saturation value, the ten seismic and ten seismoelectric records were stacked in order to improve the signal to noise ratio.

### 3.3 Example of measured seismic and seismoelectric data

An example of seismic and seismoelectric data recorded at the beginning of the third drainage ( $S_w \simeq 0.9$ ) is presented in Fig. 6 for various offsets. An offset is defined as the distance between the source and the receiver (the accelerometer or the first electrode). It appears from the comparison of Fig. 6 c) and d) that, as expected, seismoelectric data are very sensitive to electromagnetic ambient noise. For each recorded signal, the signal to noise ratio (Fig. 6 e) and f)) is computed as  $S/N = 10 \log(A_{\text{sig}}/A_{\text{noise}})^2$ , the amplitude of the signal  $A_{\text{sig}}$  being defined as its maximum value during the first ten milliseconds after triggering, and the noise amplitude  $A_{\text{noise}}$  being defined as the maximum value of the data before triggering.

All seismic records contain classically different types of seismic waves corresponding to direct, reflected and/or refracted waves. The seismic record in Fig. 6 c) shows fortunately very clear first arrivals up to an offset of 80 cm, with  $S/N$  higher than 100 dB as shown in Fig. 6 e). As claimed in Barrière et al. (2012), these first seismic arrivals were considered as direct P-waves. The very low  $S/N$  measured on seismoelectric data (lower than 5 dB in Fig. 6 f)) implies that waveforms were much more difficult to identify than in seismic signals. The first seismoelectric wave-type signal could indeed be clearly distinguished only on the three first records (offsets 20, 30, 40 cm) in Fig. 6 d).

We notice in Fig. 6 c) that the first seismic arrivals have a negative polarity consistently with what was expected from the accelerometers specifications (see Part 3.1). The measured coseismic electric field in Fig. 6 d) also presents a first negative signal implying that the corresponding  $E/\ddot{U}$  ratio is positive for the direct P-waves propagating in the partially saturated sand, which is consistent with the theoretical predictions developed in Part 2.3 (see Fig. 3 with a phase angle near zero for  $\psi_P$ ).

[Figure 6 about here.]

The recorded seismic and seismoelectric signals during the third drainage ( $S_w$  decreasing from 0.88 to 0.24) at offset = 20 cm are shown in Fig. 7. In Fig. 7 a), seismic and seismoelectric traces are normalized in order to perform a qualitative comparison of both signals during first arrivals. It

appears clearly that the frequency content of seismic and seismoelectric signals are rather different. This observation calls for the use of a time-frequency analysis in order to characterize seismic and seismoelectric attributes. We proceed the data in the following by using a Continuous Wavelet Transform which in turn will provide amplitudes, frequencies and velocities from the first arrival of seismic and seismoelectric measurements.

[Figure 7 about here.]

#### 4 ANALYSIS OF FIRST SEISMIC AND SEISMOELECTRIC ARRIVALS

We have presented in Part 2 an analytical formulation of the transfer function giving the amplitudes of seismoelectric fields induced by a seismic wave traveling in a porous medium. These transfer functions were given in particular for P and S direct body waves. Barrière et al. (2012) performed a 2D numerical simulation of waves propagation in the present experiment and showed that the first arrivals as shown in Fig. 6 c) were indeed direct P-waves, not disturbed by reflected, refracted nor surface waves.

In order to analyse the frequency content of these first P-waves arrivals, we chose to perform a spectral analysis on the first envelope or “lobe” by using a Continuous Wavelet Transform (CWT) (Daubechies 1992; Mallat & Zhong 1992). *This processing is detailed in Appendix B.3.* From typical  $C(a, b)$  map obtained by CWT, we can extract the following informations concerning the first arrivals:

- the main frequency of the first arrival, by picking the scale corresponding to the maximum of  $C(a, b)$ . The picked scale in Fig. 13 b) was converted in frequency using eq. (B6). The function converting scales into frequencies is shown in Fig. 13 c). The local spectrum can also be estimated from CWT by extracting local maxima in the time window corresponding to the first arrival (highlighted band in Fig. 13 b));
- the time at the maximum of  $C(a, b)$  in a time window corresponding to the first arrival. From that time we will deduce the propagation time of the first arrival, by subtracting a quarter period corresponding to the main frequency;



- the amplitude of the first arrival by picking the maximum amplitude of the wavelet coefficient in the  $C(a, b)$  map.

The CWT using a Mexican hat wavelet, shown as an example here, was performed on all seismic and seismoelectric datasets. We focus in the following on the results of cycle 3 (imbibition and drainage written respectively I3 and D3).

#### 4.1 Seismic and seismoelectric velocities

The apparent velocity of seismic and seismoelectric fields are deduced from the analysis of  $C(a, b)$  maps. We picked the main frequency (see Part 4.2) and the corresponding time for all measurements, and then subtracted to that picked time a quarter period at the main frequency in order to get a precise estimation of the absolute “first break” time. For a given experiment, this time determination is performed for all offsets. The apparent velocity for seismic and seismoelectric data is then deduced by a linear regression of all these first break times *vs* distances. Only the first three positions (offsets) were used since the seismoelectric data became too noisy after offset 0.4 m. We found that the described apparent velocity determination technique was well suited for seismoelectric measurements which first breaks were not always very clear in the raw data (see for example Fig. 6e)).

A compilation of seismic and seismoelectric apparent velocities measured during the third cycle is shown in Fig. 8 as a function of saturation  $S_w$ . At first order, a rather constant mean apparent velocity for seismic and seismoelectric fields was found lower than 200 m/s (between 140 and 180 m/s) during both drainage and imbibition. Nearly identical velocities in seismic and in seismoelectric demonstrates the expected coseismic origin of the seismoelectric data measured experimentally.

Barrière et al. (2012) monitored the phase velocity during imbibition and drainage also in the CWT domain by using a complex “Morlet” instead of a real “Mexican hat” wavelet used in the present study. The method consisted in picking time shifts both in amplitude and in phase spectra, and in deducing the corresponding phase velocity. Here, our simplified procedure using a real “Mexican hat” wavelet, chosen because it appears the more adapted to describe the studied first

lobe of the signal, gave results comparable to those of Barrière et al. (2012) in terms of velocity values of the direct P-waves.

[Figure 8 about here.]

## 4.2 Frequency content of seismic and seismoelectric fields

Main frequencies obtained by CWT in seismic and seismoelectric data during the third cycle are presented in Fig. 9. The first observation is that main frequencies globally decrease as a function of an increasing offset, either in seismic or in seismoelectric fields: that is understood as a classic attenuation effect of the higher frequencies. A second common characteristic in seismic and seismoelectric frequencies (Fig. 9 a) to d)) is a decrease of frequencies as a function of an increasing water saturation  $S_w$ . That trend, already observed by Barriere (2011) in a purely seismic context, was attributed to Biot's losses attenuation combined to effective permeability effects.

It appears systematically in Fig. 9 that for a given water saturation, the main frequency of the first seismic lobe is higher than the counterpart seismoelectric first lobe frequency; seismic frequencies remain for example always about twice higher than the seismoelectric frequencies at offset 0.2 m. These gaps in frequency cannot be explained by the low frequency transfer functions ( $\psi_0$  and  $\psi_{P-1f}$ ) since the latter assume that seismic and seismoelectric signals are linearly dependent in time and frequency (see eq. (A8) in Appendix A). In other words, the low frequency transfer function derived from Pride's model extended to the effective fluid presented in Part 2.2 can not account for all the seismic and seismoelectric main frequencies discrepancies observed in Fig. 9, especially when the measured frequency is lower than the Biot's frequency (correspond in Fig. 9 to  $S_w \gtrsim 0.6$ ). Some data in Fig. 9 are well above the Biot's frequency and dynamic effect are probably coming into play in the transfer function between seismic and seismoelectric fields. At least qualitatively, we may infer from Fig. 9 that the frequency content would be modified when the measured frequency crosses the Biot's frequency, corresponding to changes in attenuation mechanisms (inertial or viscous flows).

Computations performed in Part 2.2 showed that we expect a decrease of the magnitude of the ratio  $|\mathbf{E}/\ddot{\mathbf{U}}|$  as a function of the frequency, for a given  $S_w$ , when the main seismic fre-

quency exceeds the Biot's frequency (follow a vertical direction in Fig. 3 a) for a given  $S_w$ ). More precisely, we estimate from these computations that  $|\psi_{\text{P-dyn}}(0.6 \text{ kHz})| / |\psi_{\text{P-lf}}| \simeq 0.85$  when  $|\psi_{\text{P-dyn}}(1.5 \text{ kHz})| / |\psi_{\text{P-lf}}| \simeq 0.55$  for  $S_w = 0.6$ : we then expect experimentally the magnitude of the transfer function  $|\psi_{\text{P-dyn}}|$  to decrease for  $f$  above the Biot's frequency (at a given  $S_w$ ), meaning that the seismic amplitudes at a given frequency should decrease less rapidly than the seismoelectric amplitudes at that same frequency. We can not conclude in Fig. 9 if this trend is observed since only the main frequencies are shown and that seismic and seismoelectric main frequencies do not overlap; we will discuss this point further in Part 4.3.

The strong difference in dominating frequency between seismic and seismoelectric signals mentioned above is a quite common observation in laboratory measurements (Zhu & Toksöz 2003; Bordes et al. 2006, 2008) as well as in seismoelectric surveys, even at seismic frequencies much lower than the Biot's frequency (Strahser et al. 2007; Dupuis et al. 2009). Since large dipoles are strongly disturbed by electromagnetic noise, authors generally try to reach a compromise by improving the signal to noise ratio (Garambois 1999). Some preliminary tests showed in our case that a 10 cm dipole length was a suitable distance between electrodes, giving satisfying signal to noise ratio. Nevertheless, seismic signals, obtained with a calibrated and localised sensor, can be directly interpreted as local acceleration whereas seismoelectric measurements are indirect since they are obtained by a dipole. To our knowledge, the role of the acquisition geometry was never discussed so far, and we suspect that the dipole length might have an effect on the frequency content of the seismoelectric signal. A better understanding of the frequency mismatch between seismic and seismoelectric would require a more complete experimental and/or numerical study addressing the effect of acquisition geometry on seismoelectric frequency content which was not our initial purpose.

[Figure 9 about here.]

### 4.3 Amplitudes ratios

The maximum amplitude of the first arrival in seismic and seismoelectric experiments during cycle 3 are shown in Fig. 10. These amplitudes were directly extracted from the signal in time by picking

the maximum of the first lobe. As expected, measured amplitudes decrease as a function of offset and decrease also as a function of water saturation in the range  $S_w = [0.2 - 0.9]$ , consistently with previous observations of Parkhomenko & Tsze-San (1964) for seismoelectric measurements and Barrière et al. (2012) for seismic measurements. These absolute amplitudes can not be however directly interpreted in term of seismoelectric coupling since, for example, the seismic amplitudes strongly depend on seismic attenuation. That is why the transfer functions built upon a ratio of a co-seismic to a seismic field, can precisely be seen as a direct measurement of seismoelectric coupling.

[Figure 10 about here.]

In order to derive experimental transfer functions from our data, we start with a “static” approach consisting in directly computing the ratio of the seismoelectric to seismic maximum amplitudes: this procedure assumes that the transfer function does not depend on frequency although measured seismic and seismoelectric main frequencies are significantly different (see Part 4.2). These ratio  $|\mathbf{E}/\ddot{\mathbf{U}}|_{\text{exp}}$  are presented in Fig. 11 for the experiments performed during the third cycle. We have obtained these ratio by two independent ways: the first technique called “Time-static” in Figure 11 a) and b) is obtained from the data picked in time signals (shown in Fig. 10). The second technique, labelled “CWT-static” in Figure 11 b) and d), consists in picking the amplitudes of the first arrival (respectively in seismoelectric and in seismic signals) associated to the main frequency obtained by CWT (see Part 4.2) and then perform the ratio.

The two independent techniques of measurement of  $|\mathbf{E}/\ddot{\mathbf{U}}|_{\text{exp}}$  lead to the same conclusion: the ratio of seismoelectric to seismic signals is at first order constant as function of the saturation  $S_w$  for a given offset in the explored range  $S_w = [0.2 - 0.9]$ . In terms of order of magnitude, the mean  $|\mathbf{E}/\ddot{\mathbf{U}}|_{\text{exp}}$  is about  $4 \times 10^{-4} \pm 25\%$ . Although the two techniques are rather different, one processing the data in the time domain and the other one in the CWT, the differences in the ratios remain as small as  $\sim 10$  to  $25\%$  (comparison of Fig. 10 a) with Fig. 11 c), and Fig. 11 with Fig. 11 d)).

These results can also be compared to the theoretical transfer function discussed in Part 2.3. The continuous and dashed lines in Fig. 11 are obtained by computing the  $|\psi_{\text{P-If}}(S_w)|$  with

the three electrokinetics models presented in Table 2. Nevertheless, the models are computed by considering an electrokinetic coefficient 2 times smaller compared to the theoretical  $C_{ek}$  computed in Appendix A, which were based on the  $C_{ek}(S_w) = 1$  values measured by Guichet et al. (2003) (here we use  $C_{ek}(S_w = 1)/2$ ). It appears from Fig. 11 that amplitude ratios as a function of the saturation are well reproduced by the capillary tubes model of Jackson (2010) (plateau) whereas the increase predicted by Guichet et al. (2003) and Revil et al. (2007) is not retrieved in the data.

[Figure 11 about here.]

The comparison of an "experimental transfer function" with the dynamical transfer functions predictions seen in Part 2 would require to perform spectra ratios on a broad-band frequency range; the analysis of both amplitude and phase of spectra ratios could lead to a discussion on the validity of the dynamic transfer function. Unfortunately, in the present experiment, the explored frequency range is too narrow and such a complete analysis is out of reach. An alternative approach consists in calculating amplitude ratios extracted from the  $C(a, b)$  maps at the main frequency or at a frequency in the vicinity of the main frequency. The "dynamic" approach consists in picking the maximum amplitude at the main frequency in seismoelectric data (shown in Fig. 10 c) and d), and, thereafter, in picking the counterpart seismic amplitude at that same seismoelectric main frequency (denoted SEMF, "SeismoElectric Main Frequency") in the  $C(a, b)$  maps. We then perform the ratio between those amplitudes for all experiments at various saturation and obtain the results in Fig. 12. Similarly to the "static" approach shown in Fig. 11, it results that those ratios, for a given offset, are nearly constant as a function of saturation with a mean value  $5 \times 10^{-4} \pm 25\%$ . The data in Fig. 12 can be compared to the theoretical prediction of the dynamical transfer function  $|\psi_{P-dyn}(S_w)|$  using the Jackson (2010) model with an electrokinetic coefficient equal to  $C_{ek}(S_w = 1)/2$ . Since the working frequencies in the experiments are close to the Biot's frequency, as discussed in part 2.3, the theoretical dynamical transfer functions are significantly different in amplitudes compared to static ones: the dynamical transfer functions are closer to the data than the static ones.

Our "static" and "dynamic" approaches of the experimental data demonstrate that for given offset, the ratio  $|\mathbf{E}/\ddot{\mathbf{U}}|_{\text{exp}}$  remain nearly constant during the experiments even if the range of variation  $S_w = [0.2 - 0.9]$  is quite large. This global trend is particularly well recovered by the

Jackson's model (2010) coupled to the extended theory of Pride (1994) to a partially saturated fluid. More quantitatively, there is however a mismatch in terms of amplitude of the ratio  $|\mathbf{E}/\ddot{\mathbf{U}}|$ : the theoretical predictions are systematically much lower than the experimental data, about a factor 4 when the static approach is used and about a factor 2 when the dynamic approach is used. This mismatch could originate from an overestimation of electrokinetic coefficient  $C_{ek}$  (see Appendix B) or from our choice of dipole length. Indeed, we observe that the dipole length can modify the amplitude of the measured  $E$  field by a coefficient ranging 1.5 to 4, but not depending on the saturation.

[Figure 12 about here.]

## 5 CONCLUSION

Pride & Haartsen (1996) wrote the expressions of transfer functions from seismic to seismoelectric fields in a saturated porous medium. Later, Garambois & Dietrich (2001) proposed a simplified low frequency transfer function applicable when seismic frequencies are below Biot's frequency. Both studies were performed in a saturated porous media. We have generalized the transfer functions formulations to a partially saturated porous medium and have consequently derived analytical expressions of dynamic and low frequency transfer functions for P and S-waves, respectively  $\psi_{P-dyn}(S_w, \omega)$ ,  $\psi_{P-lf}(S_w)$  and  $\psi_{S-dyn}(S_w, \omega)$ ,  $\psi_{S-lf}(S_w, \omega)$ . The generalization to partially saturated medium was done using an effective fluid model under various hypotheses; we have in particular neglected the surface conductivities and used characteristic models of variations of the electrokinetic coupling  $C_{ek}$  as a function of the partial saturation  $S_w$ . In this study, we have particularly emphasized the model proposed by Jackson (2010). The effective fluid model also assumes that the seismic wavelengths are larger than the fluid heterogeneities.

The theoretical P-waves transfer functions showed significant variations in magnitude *vs* saturation and *vs* frequency. For a given frequency, the magnitude  $|\psi_{P-dyn}(S_w)|$  increases in the typical range  $S_w = [0.2-0.4]$  but is predicted to be nearly constant in the  $S_w = [0.4-0.9]$  range. For a given saturation,  $|\psi_{P-dyn}(f)|$  *vs* frequency is firstly constant before rapidly decreasing once we exceed Biot's frequency. The variation of  $|\psi_{P-dyn}(S_w, \omega)|$  is of the order 10 in the considered

range ( $S_w = [0.2-0.9]$ ,  $f = [10-10^4]$  Hz) and depends both on the used model for  $C_{ek}(S_w)$  and on the chosen frequency. We have also shown numerically that the magnitude of the P-waves low frequency transfer functions follows closely the dynamic one when  $f \leq f_c$ . We also showed that the low frequency transfer function may be carefully simplified in partially saturated media since excessive simplification introduces errors on phase predictions at highest saturations. Finally, we confirmed that the transfer function of the shear S-waves is tiny compared to the P-waves case; we concluded that the S-waves transfer functions may not be used either in experimental or numerical conditions.

We have then compared our theoretical predictions to data recorded in a partially saturated tank of silica sand:  $S_w$  was monitored during experiments (drainage and imbibition), the seismic field was recorded using accelerometers while the seismoelectric field was recorded using a couple of electrodes at mid-height of the 1 m-length-scale container. We have shown using the Continuous Wavelet Transform (CWT) that the seismic field had systematically a main frequency about twice as big as the main seismoelectric frequency; that observation was true for all offsets (distance to the source).

We have also estimated the experimental ratios  $|\mathbf{E}_P(S_w)/\ddot{\mathbf{U}}_P(S_w)|$  with various methods (picking in time and CWT) and those ratios appear to be approximatively constant during the experiments in the range  $S_w = [0.2-0.9]$  for all offsets. The comparison of data with the theory led to the conclusion that the trend and the order of magnitude of the recorded experimental transfer functions is recovered by the theoretical prediction when using the Jackson (2010) model for the saturation dependence of electrokinetic coefficient. Working near the Biot's frequency in the experiments, we verified that dynamics effects come into play since the dynamic transfer function is closer to the data than the static transfer function. We have also demonstrated that the CWT processing is well suited for estimating apparent velocities, main frequencies and amplitude ratio at the main frequency of the data.

This study confirms that introducing the effective fluid model into the Pride's theory is appropriate when wavelengths are larger than the fluid heterogeneities. Nevertheless, the accuracy of the predicted transfer function strongly depends on electrokinetic models, that have to be completed

to account more precisely for the fluid distribution that can involve different fluid thicknesses with strong effects on the effective viscosity and permeability.

## 6 ACKNOWLEDGEMENTS

This study has benefited to the ANR program of the French government, especially via the TRANSEK project. The authors thanks S. Garambois, G. Sénéchal, D. Rousset for their constructive suggestions and J. Holzhauer for reading carefully the original manuscript.

## REFERENCES

- Allègre, V., Jouniaux, L., Lehmann, F., & Sailhac, P., 2010. Streaming potential dependence on water-content in fontainebleau sand, *Geophysical Journal International*, **182**(3), 1248–1266.
- Allègre, V., Lehmann, F., Ackerer, P., Jouniaux, L., & Sailhac, P., 2012. A 1-d modelling of streaming potential dependence on water content during drainage experiment in sand, *Geophysical Journal International*, **189**(1), 285–295.
- Archie, G. E., 1942. The electrical resistivity log as an aid in determining some reservoir characteristics, *Trans. Am. Inst. Min. Metall. Pet. Eng.*, (146), 54–62.
- Bachrach, R. & Nur, A., 1998. High-resolution shallow-seismic experiments in sand, part i: Water table, fluid flow, and saturation, *Geophysics*, **63**(4), 1225–1233.
- Bachrach, R., Dvorkin, J., & Nur, A., 1998. High-resolution shallow-seismic experiments in sand, part ii: Velocities in shallow unconsolidated sand, *Geophysics*, **63**(4), 1234–1240.
- Barriere, J., 2011. *Atténuation et dispersion des ondes P en milieu poreux partiellement saturé: une approche expérimentale*, PhD Thesis, Université de Pau et des Pays de l'Adour, France.
- Barrière, J., Bordes, C., Brito, D., Sénéchal, P., & Perroud, H., 2012. Laboratory monitoring of p waves in partially saturated sand, *Geophysical Journal International*, **191**(3), 1152–1170.
- Berryman, J. G., 1981. Elastic wave propagation in fluid-saturated porous media, *Acoustical Society of America Journal*, **69**, 416–424.
- Biot, M. A., 1956a. Theory of propagation of elastic waves in a fluid-saturated porous solid: I. low frequency range, *J. Acoust. Soc. Am.*, **28**(2), 168–178.
- Biot, M. A., 1956b. Theory of propagation of elastic waves in a fluid-saturated porous solid: II. high frequency range, *J. Acoust. Soc. Am.*, **28**(2), 178–191.
- Biot, M. A., 1962. Mechanics of deformation and acoustic propagation in porous media, *J. Appl. Phys.*, **34**(1), 36–40.



- Block, G. I. & Harris, J. G., 2006. Conductivity dependence of seismoelectric wave phenomena in fluid-saturated sediments, *Journal of Geophysical Research: Solid Earth (1978–2012)*, **111**(B1).
- Bordes, C., Jouniaux, L., Dietrich, M., Pozzi, J.-P., & Garambois, S., 2006. First laboratory measurements of seismo-magnetic conversions in fluid-filled fontainebleau sand, *Geophysical Research Letters*, **33**(1).
- Bordes, C., Jouniaux, L., Garambois, S., Dietrich, M., Pozzi, J.-P., & Gaffet, S., 2008. Evidence of the theoretically predicted seismo-magnetic conversion, *Geophysical Journal International*, **174**(2), 489–504.
- Butler, K. E. & Russell, R. D., 1993. Subtraction of powerline harmonics from geophysical records, *Geophysics*, **58**(6), 898–903.
- Carcione, J. M., 2001. *Wave fields in real media : Wave propagation in anelastic, anisotropic and porous media*, Pergamon, Elsevier Science Ltd.
- Chen, B. & Mu, Y., 2005. Experimental studies of seismoelectric effects in fluid-saturated porous media, *Journal of Geophysics and Engineering*, **2**(3), 222–230.
- Darnet, M. & Marquis, G., 2004. Modelling streaming potential (sp) signals induced by water movement in the vadose zone, *Journal of hydrology*, **285**(1), 114–124.
- Daubechies, I., 1992. Ten lectures on wavelets, *CBMS NSF Regional Conference Series in Applied Mathematics (Philadelphia: SIAM)*.
- Doussan, C. & Ruy, S., 2009. Prediction of unsaturated soil hydraulic conductivity with electrical conductivity, *Water resources research*, **45**(10).
- Dukhin, A., Goetz, P., & Thommes, M., 2010. Seismoelectric effect: A non-isochoric streaming current. 1. experiment, *Journal of colloid and interface science*, **345**(2), 547–553.
- Dupuis, J., Butler, K., Kopic, A., & Harris, B., 2009. Anatomy of a seismoelectric conversion: Measurements and conceptual modeling in boreholes penetrating a sandy aquifer, *Journal of Geophysical Research*, **114**(B10), B10306.
- Dupuis, J. C. & Butler, K. E., 2006. Vertical seismoelectric profiling in a borehole penetrating glaciofluvial sediments, *Geophys. Res. Lett.*, **33**(16).
- Dupuis, J. C., Butler, K. E., & Kopic, A. W., 2007. Seismoelectric imaging of the vadose zone of a sand aquifer, *Geophysics*, **72**, A81–A85.
- Frenkel, J., 1944. On the theory of seismic and electroseismic phenomena in a moist soil., *J. Phys.*, **8**(4), 230–241.
- Garambois, S., 1999. *Etudes expérimentales et théoriques des conversions d'ondes sismo-électriques dans les milieux poreux superficiels*, Ph.D. thesis, Université Joseph Fourier, Grenoble 1.
- Garambois, S. & Dietrich, M., 2001. Seismoelectric wave conversions in porous media: Field measurements and transfer function analysis, *Geophysics*, **66**(5), 1417–1430.
- Garambois, S. & Dietrich, M., 2002. Full waveform numerical simulations of seismoelectromagnetic wave

- conversions in fluid-saturated stratified porous media., *J. Geophys. Res.*, **107**(B7).
- Glover, P., 1998. Nature of surface electrical conductivity sandstones, and clays, *Geophysical Research Letters*, **25**(5), 691–694.
- Guan, W. & Hu, H., 2008. Finite-difference modeling of the electroseismic logging in a fluid-saturated porous formation, *Journal of computational physics*, **227**(11), 5633–5648.
- Guichet, X., Jouniaux, L., & Pozzi, J.-P., 2003. Streaming potential of a sand column in partial saturation conditions, *J. Geophys. Res.*, **108**(B3).
- Guichet, X., Jouniaux, L., & Catel, N., 2006. Modification of streaming potential by precipitation of calcite in a sandwater system: laboratory measurements in the ph range from 4 to 12, *Geophys. J. Int.*, **166**.
- Haines, S. S., Guitton, A., & Biondi, B., 2007a. Seismoelectric data processing for surface surveys of shallow targets, *Geophysics*, **72**, G1–G8.
- Haines, S. S., Pride, S. R., Klemperer, S. L., & Biondi, B., 2007b. Seismoelectric imaging of shallow targets, *Geophysics*, **72**, G9–G20.
- Jackson, M., 2010. Multiphase electrokinetic coupling: Insights into the impact of fluid and charge distribution at the pore scale from a bundle of capillary tubes model, *Journal of Geophysical Research*, **115**(B7), B07206.
- Jougnot, D., Linde, N., Revil, A., & Doussan, C., 2012. Derivation of soil-specific streaming potential electrical parameters from hydrodynamic characteristics of partially saturated soils, *Vadose Zone Journal*, **11**(1).
- Jougnot, D., Rubino, J. G., Carbajal, M. R., Linde, N., & Holliger, K., 2013. Seismoelectric effects due to mesoscopic heterogeneities, *Geophysical Research Letters*, pp. n/a–n/a.
- Jouniaux, L. & Pozzi, J.-P., 1995. Streaming potential and permeability of saturated sandstones under triaxial stress: consequences for electrotelluric anomalies prior to earthquakes, *J. Geophys. Res.*, **100**, 10,197–10,209.
- Kulesa, B., Murray, T., & Rippin, D., 2006. Active seismoelectric exploration of glaciers, *Geophys. Res. Lett.*, **33**, L07503.
- Kumar, P. & Foufoula-Georgiou, E., 1997. Wavelet analysis for geophysical applications, *Reviews of Geophysics*, **35**(4), 385–412.
- Lebedev, M., Toms-Stewart, J., Clennell, B., Pervukhina, M., Shulakova, V., Paterson, L., M., M. T., Gurevich, B., & Wenzlau, F., 2009. Direct laboratory observation of patchy saturation and its effects on ultrasonic velocities, *The Leading Edge*, **28**(1), 24–27.
- Lo, W., Sposito, G., & Majer, E., 2005. Wave propagation through elastic porous media containing two immiscible fluids, *Water Resources Research*, **41**, 2025.
- Mallat, S. & Zhong, S., 1992. Characterization of signals from multiscale edges, *IEEE Trans. Pattern Anal. Mach. Intell.*, **14**(7), 710–732.

- Masson, Y. J. & Pride, S. R., 2007. Poroelastic finite difference modeling of seismic attenuation and dispersion due to mesoscopic-scale heterogeneity, *Journal of Geophysical Research (Solid Earth)*, **112**, 3204.
- Mavko, G. & Nolen-Hoeksema, R., 1994. Estimating seismic velocities at ultrasonic frequencies in partially saturated rocks., *Geophysics*, **59**(2), 252–258.
- Parkhomenko, I. & Tsze-San, C., 1964. A study of the influence of moisture on the magnitude of the seismoelectric effect in sedimentary rocks by a laboratory method, *Bull. (Izv.) Acad. Sci., USSR, Geophys. Ser.*, pp. 115–118.
- Perrier, V., Philipovitch, T., & Basdevant, C., 1995. Wavelet spectra compared to fourier spectra, *Journal of Mathematical Physics*, **36**, 1506–1519.
- Pride, S., 1994. Governing equations for the coupled electromagnetics and acoustics of porous media, *Physical Review B*, **50**, 15678–15695.
- Pride, S. & Haartsen, M. W., 1996. Electro seismic wave properties, *J. Acoust. Soc. Am.*, **100**, 1301–1315.
- Reppert, P. M., Morgan, F. D., Lesmes, D. P., & Jouniaux, L., 2001. Frequency-dependent streaming potentials, *Journal of Colloid and Interface Science*, (234), 194–203.
- Revil, A. & Cerepi, A., 2004. Streaming potentials in two-phase flow conditions, *Geophysical research letters*, **31**(11).
- Revil, A. & Jardani, A., 2010. Seismoelectric response of heavy oil reservoirs: theory and numerical modelling, *Geophysical Journal International*, **180**(2), 781–797.
- Revil, A. & Mahardika, H., 2013. Coupled hydromechanical and electromagnetic disturbances in unsaturated porous materials, *Water resources research*, **49**(2), 744–766.
- Revil, A., Linde, N., Cerepi, A., Jougnot, D., Matthäi, S., & Finsterle, S., 2007. Electrokinetic coupling in unsaturated porous media, *J. Colloid Interface Sci.*, **313**, 315–327.
- Revil, A., Barnier, G., Karaoulis, M., Sava, P., Jardani, A., & Kulesa, B., 2014. Seismoelectric coupling in unsaturated porous media: theory, petrophysics, and saturation front localization using an electroacoustic approach, *Geophysical Journal International*, **196**(2), 867–884.
- Rubino, J. G. & Holliger, K., 2012. Seismic attenuation and velocity dispersion in heterogeneous partially saturated porous rocks, *Geophysical Journal International*, **188**, 1088–1102.
- Santos, J., Zyserman, F., & Gauzellino, P., 2011. Numerical electro seismic modeling: A finite element approach, *Applied Mathematics and Computation*.
- Santos, J. E., Douglas, Jr., J., Corberó, J., & Lovera, O. M., 1990. A model for wave propagation in a porous medium saturated by a two-phase fluid, *Acoustical Society of America Journal*, **87**, 1439–1448.
- Schakel, M. & Smeulders, D., 2010. Seismoelectric reflection and transmission at a fluid/porous-medium interface, *The Journal of the Acoustical Society of America*, **127**, 13.
- Schakel, M., Smeulders, D., Slob, E., & Heller, H., 2011a. Seismoelectric interface response: experimental

- results and forward model, *Geophysics*, **76**(4), N29–N36.
- Schakel, M., Smeulders, D., Slob, E., & Heller, H., 2011b. Laboratory measurements and theoretical modeling of seismoelectric interface response and coseismic wave fields, *Journal of Applied Physics*, **109**(7), 074903–074903.
- Sénéchal, P., Garambois, S., & Bordes, C., 2010. Feasibility of acoustic imaging for in-situ characterization of subsurface soil injected with fresh mortar, *Journal of Applied Geophysics*, **72**(3), 184–193.
- Strahser, M., Jouniaux, L., Sailhac, P., Matthey, P.-D., & Zillmer, M., 2011. Dependence of seismoelectric amplitudes on water content, *Geophysical Journal International*, **187**(3), 1378–1392.
- Strahser, M. H., Rabbel, W., & Schildknecht, F., 2007. Polarisation and slowness of seismoelectric signals: a case study, *Near Surface Geophysics*, **5**(2), 97–114.
- Tardif, E., Glover, P. W., & Ruel, J., 2011. Frequency-dependent streaming potential of ottawa sand, *Journal of Geophysical Research: Solid Earth (1978–2012)*, **116**(B4).
- Teja, A. S. & Rice, P., 1981. Generalized corresponding states method for viscosities of liquid mixtures, *Industrial Engineering Chemistry Fundamentals*, **20**, 77–81.
- Thompson, A. H. & Gist, G. A., 1993. Geophysical applications of electrokinetic conversion, *The Leading Edge*, **12**, 1169–1173.
- Tuncay, K. & Corapcioglu, M. Y., 1996. Body waves in poroelastic media saturated by two immiscible fluids, *jgr*, **101**, 25149–25160.
- Walton, K., 1987. The effective elastic moduli of a random packing of spheres, *Journal of Mechanics Physics of Solids*, **35**, 213–226.
- Warden, S., Garambois, S., Sailhac, P., Jouniaux, L., & Bano, M., 2012. Curvet-based seismoelectric data processing, *Geophysical Journal International*, **190**(3), 1533–1550.
- Warden, S., Garambois, S., Jouniaux, L., Brito, D., Sailhac, P., & Bordes, C., 2013. Seismoelectric wave propagation numerical modelling in partially saturated materials, *Geophysical Journal International*, **194**(3), 1498–1513.
- Zhu, Z. & Toksöz, M. N., 2003. Crosshole seismoelectric measurements in borehole models with fractures, *Geophysics*, **68**(5), 1519–1524.
- Zhu, Z. & Toksöz, M. N., 2005. Seismoelectric and seismomagnetic measurements in fractured borehole models, *Geophysics*, **70**(4), F45–F51.
- Zhu, Z., Haartsen, M. W., & Toksöz, M., 2000. Experimental studies of seismoelectric conversions in fluid-saturated porous media, *Journal of Geophysical Research: Solid Earth (1978–2012)*, **105**(B12), 28055–28064.
- Zyserman, F. I., Gauzellino, P. M., & Santos, J. E., 2010. Finite element modeling of shte and psvtm electroseismics, *Journal of Applied Geophysics*, **72**(2), 79–91.
- Zyserman, F. I., Gauzellino, P. M., & Santos, J. E., 2012. Numerical evidence of gas hydrate detection by

means of electroseismics, *Journal of Applied Geophysics*, **86**(0), 98 – 108.

## **Appendix A DYNAMIC TRANSFER FORMULATION AS A FUNCTION OF SATURATION $S_w$**

We present the set of equations used in our analytical calculations of dynamic and low frequency transfer functions. These equations are derived from the original work of Pride (1994) and Pride & Haartsen (1996) whose formulations were written for a fluid-filled porous medium. We extend Pride's models to a partially fluid saturated medium using an effective model, the main assumption being that we are dealing with seismic waves which wavelengths are much larger than fluid heterogeneities. We follow a similar approach to what has been done in Garambois & Dietrich (2001); Barrière et al. (2012); Warden et al. (2013).

The input parameters are defined and listed in Tables 1 and 3:

- Fluid:  $\rho_w, \eta_w, K_w, \sigma_w, \rho_g, \eta_g, K_g$ , (7 parameters)
- Solid:  $\rho_s, K_s$ , (2 parameters)
- Porous medium:  $\phi, k_0, \gamma_0, K_D, G, C_{ek}(S_w = 1), f(S_w), m, n$ . (9 parameters)

where subscripts  $w$  and  $g$  respectively refer to water and gas. These parameters are then combined to lead to the dynamic and low frequency transfer functions for P and S-waves derived below.

The variation of the poroelastic moduli of the medium  $H, M, C$  vs water saturation saturation

$S_w$  are computed using a combination of parameters including  $K_f$ ,  $B$ ,  $K_U$ , following:

$$\begin{aligned}
K_f(S_w) &= 1 / \left( \frac{S_w}{K_w} + \frac{1 - S_w}{K_g} \right), \\
B(S_w) &= \frac{1/K_D - 1/K_s}{1/K_D - 1/K_s + \phi(1/K_f(S_w) - 1/K_s)}, \\
K_U(S_w) &= \frac{K_D}{1 - B(S_w)(1 - K_D/K_s)}, \\
C(S_w) &= B(S_w)K_U(S_w), \\
\alpha(S_w) &= \frac{1 - K_D/K_U(S_w)}{B(S_w)}, \\
M(S_w) &= \frac{B(S_w)K_U(S_w)}{\alpha(S_w)}, \\
H(S_w) &= K_U(S_w) + \frac{4}{3}G.
\end{aligned} \tag{A1}$$

The effective fluid density and the bulk density of the porous medium are respectively computed as follows:

$$\begin{aligned}
\rho_f(S_w) &= (1 - S_w)\rho_g + S_w\rho_w, \\
\rho(S_w) &= \phi\rho_f(S_w) + (1 - \phi)\rho_s,
\end{aligned}$$

while the effective fluid viscosity is expressed by the Teja & Rice (1981) relation:

$$\eta_f(S_w) = \eta_g \left( \frac{\eta_w}{\eta_g} \right)^{S_w}. \tag{A2}$$

Neglecting surface conductivities, we use the effective electrical conductivity of the porous medium :

$$\sigma(S_w) = \frac{\phi\sigma_w}{\gamma_0 S_w^{-n}}, \tag{A3}$$

where  $n$  is the second Archie's coefficient. The frequency dependent dynamic permeability  $k$ , effective density  $\tilde{\rho}$ , complex density  $\rho_t$  and effective electrical permittivity  $\tilde{\epsilon}$  are respectively com-

puted as:

$$\begin{aligned}
k(S_w, \omega) &= k_0 \left[ \left( 1 - i \frac{\omega}{\omega_c(S_w)} \frac{4}{m} \right)^{\frac{1}{2}} - i \frac{\omega}{\omega_c(S_w)} \right]^{-1}, \\
\tilde{\rho}(S_w, \omega) &= \frac{i}{\omega} \frac{\eta(S_w)}{k(S_w, \omega)}, \\
\rho_t(S_w, \omega) &= \rho(S_w) - \frac{\rho_f^2(S_w)}{\tilde{\rho}(S_w, \omega)}, \\
\tilde{\varepsilon}(\omega) &= \frac{i}{\omega} \sigma(S_w).
\end{aligned} \tag{A4}$$

The frequency dependent electro-kinetic coupling coefficient  $L$  is computed as:

$$\begin{aligned}
L(S_w, \omega) &= L_0(S_w) \left[ 1 - i \frac{\omega}{\omega_c(S_w)} \frac{m}{4} \right]^{-\frac{1}{2}} \\
&= -\frac{\phi}{\gamma_0} \sigma_w S_w^n C_{ek}(S_w = 1) f(S_w) \left[ 1 - i \frac{\omega}{\omega_c(S_w)} \frac{m}{4} \right]^{-\frac{1}{2}},
\end{aligned} \tag{A5}$$

where the Biot critical pulsation  $\omega_c$  is obtained from equation 5 by the relation  $\omega_c = 2\pi f_c$  and  $f(S_w)$  are given in Appendix B for various models.

In the following, the dependance of the parameters to  $S_w$  and  $\omega$  are not all explicitly written for clarity. The slowness of the fast P-waves  $s_P$  and the slowness of the S-waves  $s_S$  are respectively computed as :

$$\begin{aligned}
s_P(S_w, \omega) &= \left[ \frac{1}{2} \gamma - \frac{1}{2} \sqrt{\gamma^2 - \frac{4\tilde{\rho}\rho}{MH - C^2} \left( \frac{\rho_t}{\rho} + \frac{\tilde{\rho}L^2}{\tilde{\varepsilon}} \right)} \right]^{1/2}, \\
s_S(S_w, \omega) &= \left[ \frac{1}{2} \frac{\rho_t}{G} + \frac{1}{2} \mu \tilde{\varepsilon} \left( 1 + \frac{\tilde{\rho}L^2}{\tilde{\varepsilon}} \right) \right. \\
&\quad \left. + \frac{1}{2} \sqrt{\left[ \frac{\rho_t}{G} - \mu \tilde{\varepsilon} \left( 1 + \frac{\tilde{\rho}L^2}{\tilde{\varepsilon}} \right) \right]^2 - 4\mu \frac{\rho_f^2 L^2}{G}} \right]^{1/2}
\end{aligned} \tag{A6}$$

$$\text{with } \gamma(S_w, \omega) = \frac{\rho M + \tilde{\rho} H (1 + \tilde{\rho} L^2 / \tilde{\varepsilon}) - 2\rho_f C}{HM - C^2}.$$

Lastly, the dynamic transfer function for P and S-waves, respectively  $\psi_{P\text{-dyn}}$  and  $\psi_{S\text{-dyn}}$ , are

given by:

$$\psi_{\text{P-dyn}}(S_w, \omega) = \frac{E}{\ddot{U}_P} = \left( i \frac{\tilde{\rho}L}{\omega \tilde{\varepsilon}} \right) \left( \frac{Hs_P^2 - \rho}{Cs_P^2 - \rho_f} \right), \quad (\text{A7})$$

$$\psi_{\text{S-dyn}}(S_w, \omega) = \frac{E}{\ddot{U}_S} = \left( i \frac{\mu \tilde{\rho}GL}{\omega \rho_f} \right) \left( \frac{s_S^2 - \rho/G}{s_S^2 - \mu \tilde{\varepsilon}} \right),$$

and the corresponding low frequency transfer functions  $\psi_{\text{P-lf}}$  and  $\psi_{\text{S-lf}}$  become:

$$\begin{aligned} \psi_{\text{P-lf}}(S_w) &= -C_{ek}(S_w = 1)f(S_w) \rho_f \left( 1 - \frac{\rho}{\rho_f} \frac{C}{H} \right), \\ &= \psi_0(S_w) \left( 1 - \frac{\rho}{\rho_f} \frac{C}{H} \right), \end{aligned} \quad (\text{A8})$$

$$\psi_{\text{S-lf}}(S_w, \omega) = -C_{ek}(S_w = 1)f(S_w) \rho_f \left( -i \frac{\mu}{\omega} \frac{G}{\rho} \frac{\phi}{\gamma_0} \sigma_w \right).$$

The complete set of equations (A1) to (A8) rely on a few hypotheses and approximations compared to the original Pride's formulation. Here are some justifications:

- We neglect the surface conductivities and use a reduced version of the electrical conductivity  $\sigma(S_w)$  in eq. (A3) compared to a more general expression of the dynamic electrical conductivity  $\sigma(S_w, \omega) = \frac{\phi}{\gamma_0} S_w^n \sigma_w + 2 \frac{\phi}{\gamma_0} \frac{C_{em} + C_{os}(\omega)}{\Lambda}$  (e.g. Warden et al. (2013)). Using such reduced formulation, we assume that the electromigration  $C_{em}$  and electroosmotic  $C_{os}$  conductances as defined in Pride (1994) are negligible in the calculation of the dynamic electrical conductivity, as stated in Garambois & Dietrich (2001).

- We use a reduced version of the effective electrical permittivity  $\tilde{\varepsilon}$  in eq. (A4) compared to a more general dynamic expression  $\tilde{\varepsilon}(S_w, \omega) = \varepsilon(S_w, \omega) + \frac{i}{\omega} \sigma(S_w, \omega) - \tilde{\rho}(S_w, \omega) L^2(S_w, \omega)$ . We assume that we remain in the low-frequency range and diffusive regime where  $\varepsilon(\omega) \ll \frac{i}{\omega} \sigma(\omega)$  (Garambois & Dietrich 2001). We also neglect for consistency the electroosmotic term  $\tilde{\rho}(\omega) L^2(\omega)$  in the dynamic expression.



- The static electro-coupling coefficient  $L_0$  in eq. (A5) is multiplied by  $\left(1 - 2\frac{\tilde{d}}{\Lambda}\right)$  in the Pride's version, where  $\tilde{d}$  is basically the electrical double-layer thickness and  $\Lambda$  is the pore-shape factor or nearly the radius of the pores. This prefactor in  $L_0$  is tiny (less than a tenth of a percent) in our case and is then neglected.

- The dynamic electro-kinetic coupling of (Pride 1994) is defined as

$$L(\omega) = L_0 \left[ 1 - i \frac{\omega}{\omega_c} \frac{m}{4} \left( 1 - 2\frac{\tilde{d}}{\Lambda} \right)^2 \left( 1 - i^{3/2} \frac{\tilde{d}}{\delta(\omega)} \right)^2 \right]^{-\frac{1}{2}},$$

where  $\delta$  is the skin depth. For consistency with the previous hypotheses, we have also chosen to ignore both terms in parentheses since they represent again a very tiny correction to  $L$  in eq. (A5) in the frequency band of the present study.

## Appendix B $C_{EK}$ VALUE AS A FUNCTION OF SATURATION $S_w$

### Appendix B.1 $C_{ek}$ at saturation $S_w = 1$

Guichet et al. (2003) measured experimentally the following value of the electrokinetic coefficient  $C_{ek}$  under saturated conditions in a sand very similar to the one used in the present study:

$$C_{ek}(S_w = 1) = \frac{\varepsilon_0 \varepsilon_f \zeta}{\eta_f \sigma_f} = -1.14 \times 10^{-6} \text{ V/Pa}. \quad (\text{B1})$$

The saturating fluid was water ( $\eta_f = 10^{-3} \text{ Pa}\cdot\text{s}$ ,  $\varepsilon_f \simeq 80$ ) which electrical conductivity was  $\sigma_f = \sigma_w = 1.78 \cdot 10^{-2} \text{ S/m}$ . Equation (B1) then lead to a zeta potential  $\zeta = -29 \text{ mV}$  in the sand under the experimental conditions of Guichet et al. (2003).

Since we have not performed any zeta potential measurements here, we have also used  $\zeta = -29 \text{ mV}$  for our sand in saturated conditions which lead to  $C_{ek}(S_w = 1) = -1.73 \times 10^{-6} \text{ V/Pa}$  (value used in Tables 1 and 3) for the conductivity of the electrolyte  $\sigma_w = 1.17 \times 10^{-2} \text{ S/m}$ . In this study, we used

### Appendix B.2 $C_{ek}$ vs $S_w$

We detail in the following the different models giving the dependence of  $C_{ek}$  vs  $S_w$  as listed in Table 2.

Studying Fontainebleau sand (very close to Landes sand) Guichet et al. (2003) observed an increase of electrokinetic coefficient when the drainage was obtained by injection of argon. They deduced an alternative model:

$$C_{ek}(S_w) = C_{ek}(S_w = 1)S_e, \quad (\text{B2})$$

where the effective water saturation  $S_e = (S_w - S_{w0})/(1 - S_{w0})$  depends on the residual water saturation  $S_{w0}$ .

Revil et al. (2007) proposed to express the electrokinetic coefficient as a function of the excess charge per unit of pore volume. Assuming that the surface conductivity of the rock was negligible and that the wetting phase remained continuous even for very low saturation, they proposed the following relation:

$$C_{ek}(S_w) = C_{ek}(S_w = 1) \frac{S_e^{\frac{2+3\lambda}{\lambda}}}{S_w^{n+1}} \quad (\text{B3})$$

where  $\lambda$  is the curve-shape parameter characterizing the pore space distribution ( $\lambda = 1.7$  for sands).

In order to describe the multiphase streaming potential coupling coefficients, Jackson (2010) used a bundle of capillary tubes model occupied by two immiscible phases (oil-water or gas-water systems). If water is the only phase that contains an excess of charge,  $C_{ek}(S_w)$  can be defined as:

$$C_{ek}(S_w) = C_{ek}(S_w = 1) \frac{S_e}{S_w^n}. \quad (\text{B4})$$

In this latter formulation, the residual water saturation is adjusted to  $S_{w0}$  and the surface conductivity of the rock is neglected. This model suggests that  $C_{ek}(S_w)$  may increase at partial saturation before decreasing to zero at  $S_{w0}$ . This is physically plausible in case the relative electrical conductivity decreases more rapidly than the effective water saturation. Recently, Allègre et al. (2010, 2012) confirmed that such behavior could be observed in silica sands with a very strong increase of  $C_{ek}(S_w)$  at  $S_w = 0.8$ . Such behaviour is also predicted for Fontainebleau sand by Jougnot et al. (2012) using an alternative model also based on a bundle of capillary tubes.

### Appendix B.3 On the use of the Continuous Wavelet Transform (CWT)

This data processing computes the similarity between a theoretical wavelet seen in Fig. 13 a) and a recorded signal seen in Fig. 13 b), by comparing the original signal  $s(t)$  to a shifted/compressed/stretched version of a “mother wavelet”  $w(t)$ . By calculating the cross-correlation of the signal  $s$  and the wavelet  $w$  at various scales  $a$  and positions  $b$ , we obtain the  $C(a, b)$  coefficients defined as:

$$C(a, b) = \frac{1}{\sqrt{a}} \int_{-\infty}^{\infty} s(t) w^* \left( \frac{t - b}{a} \right) dt, \quad (\text{B5})$$

where  $w^*$  is the complex conjugate of the wavelet function. The scale  $a$  is related to a pseudo-frequency  $f_a$  as seen in Fig. 13 c) by the relation:

$$f_a = \frac{f_0}{aT}, \quad (\text{B6})$$

where  $f_0$  is the central frequency of the wavelet and  $T$  the sampling period of the recorded signal.

The computed spectrum in Fig. 13 d) strongly depends on the choice of the mother wavelet and corresponds to a smoothed and stretched approximation of a Fourier spectrum. CWT cannot achieve the high frequency resolution of a Fourier transform but it can however distinguish and characterize frequency properties of singular events in non stationary signals, like in our experimental data. The best spectral resolution is obtained by using mother wavelets with a lot of vanishing moments (*i.e.* oscillations) but the time resolution obeys the opposite rule (Perrier et al. 1995); the choice of the mother wavelet is therefore a compromise between time and frequency resolution.

In the present study, we propose to use a CWT during imbibition and drainage experiments in order to monitor the main frequencies, velocities and amplitudes of the first lobe in seismic and seismoelectric signals. We used the same wavelet for all CWT computations in order to legitimate the validity of a comparison between seismic and seismoelectric attributes.

Preliminary signal processing tests led to the conclusion that the real “Mexican hat” wavelet shown in Fig. 13 a) was the most convenient wavelet to characterize in frequency the first lobe of the signal. The Mexican hat wavelet, defined as the second derivative of the gaussian function, is widely used in geophysics (Kumar & Foufoula-Georgiou 1997). As an example, we have ap-

plied the continuous Mexican hat wavelet transform to one seismic record obtained during the third drainage ( $S_w = 0.9$ ); the derived  $C(a, b)$  map is presented in Fig. 13 d).

[Figure 13 about here.]

**LIST OF FIGURES**

- 1 Magnitude a) and phase angles b) as a function of the frequency  $f$  respectively for the P-waves dynamic transfer function  $\psi_{\text{P-dyn}}$ , for the P-waves low frequency transfer function  $\psi_{\text{P-lf}}$  and for the P-waves simplified low frequency transfer function  $\psi_0$  in a saturated sand (formulation in Appendix A and physical parameters in Table 1). c) and d) are the magnitudes and phase angles of the S-waves transfer functions ( $\psi_{\text{S-dyn}}$  and  $\psi_{\text{S-lf}}$ ) for the same parameters of the computations shown in a) and b). The Biot's frequency  $f_c$  is shown with a vertical dashed line on all graphs.
- 2 Absolute values of the coupling electrokinetic coefficients  $|C_{ek}(S_w)|$  as a function of the water saturation  $S_w$ , for different electrokinetic models. The analytical formulations of the models are shown explicitly in Appendix B.
- 3 a) Magnitude of the P-waves dynamic transfer function  $|\psi_{\text{P-dyn}}(S_w, \omega)|$  as a function of frequency  $f$  and saturation  $S_w$ , based on the Jackson (2010) model for electrokinetic coupling. The white line gives Biot's frequency values as a function of  $S_w$ . b) and c): Magnitudes and phase angles as a function of the saturation  $S_w$  respectively for the P-waves dynamic transfer function  $\psi_{\text{P-dyn}}$  at  $f = 1.5$  kHz, for the P-waves low frequency transfer function  $\psi_{\text{P-lf}}$  and for the P-waves simplified low frequency transfer function  $\psi_0$  in a partially saturated silica sand. *Magnitude of dynamic transfer functions obtained with the models of Guichet et al. (2003) and Revil et al. (2007) are respectively displayed by blue and green curves.*
- 4 a) Sketch of the experimental apparatus used in the present study. b) Typical record of the seismic source signal (steel ball hitting the granite) *vs* time, recorded by an accelerometer located on the granite cylinder. c) Normalized amplitude spectrum of the source signal shown in b) as a function of frequency.
- 5 Example of water saturation measurements along the receivers array for different values of  $S_w$ . Variations of  $S_w$  between offset=0.2m and 0.4m are lower than uncertainties on  $S_w$  measurements displayed as an example at offset=0.3m, during D3, when  $S_w$  is close to 0.6.
- 6 a) View from above of the horizontal plane of the experimental set-up containing accelerometers (black squares) and capacitance probes (red rectangles). b) View from above of the same horizontal plane shown in a) containing dipoles (couple of electrodes in magenta). c) Seismic records at various offsets (source/receiver distance) obtained at the beginning of the drainage of the third cycle for  $S_w \approx 0.9$ . d) Seismoelectric record at various offsets recorded simultaneously to the seismic data shown in c). e) Signal to noise ratio of the data shown in c) *vs* offsets. f) Signal to noise ratio of the data shown in d) *vs* offsets.
- 7 a) Normalised seismic traces (grey) and seismoelectric fields (black) measured at offset = 0.2 m during the third drainage. b)  $S_w$  coefficient as a function of the experiment number shown in a).
- 8 Apparent seismic and seismoelectric velocities measured during the third cycle as a function of  $S_w$ . a), b), c) and d) are respectively the seismic velocities during imbibition (I3), seismic velocities during drainage (D3), seismoelectric velocities during imbibition and seismoelectric velocities during drainage. The error bars, around 10% of the measured velocity, originate from uncertainties on the accelerometers locations ( $\pm 5$  mm), on the picking times ( $\pm 4 \times 10^{-5}$  s) and on the dipole lengths between coupled electrodes ( $\pm 10$  mm).

9 Main frequency (picked from a CWT signal processing) obtained during the third cycle from respectively a) the seismic data during imbibition, b) the seismic data during drainage, c) the seismoelectric data during imbibition and d) seismoelectric data during drainage. All figures are shown as a function of the saturation  $S_w$  and for three different offsets: blue squares 0.2 m, green circles 0.3 m and red triangles 0.4 m. The error bars originate from uncertainties in picking pseudo frequencies ( $\pm 2$  samples around the maximum amplitude). The variations in Biot's frequency  $v_s$  saturation (computed from eq. (5) and Appendix A) during those experiments are shown with a dashed black line.

10 First arrival amplitude (picked in time signals) during the third cycle from respectively a) the seismic data during imbibition, b) the seismic data during drainage, c) the seismoelectric data during imbibition and d) seismoelectric data during drainage. All figures are shown as a function of the saturation  $S_w$  and for three different offsets: blue squares 0.2 m, green circles 0.3 m and red triangles 0.4 m. The associated error bars (around 7%) in seismic and seismoelectric amplitudes originate from uncertainties in the receivers location ( $\pm 5$  mm), in the dipole length ( $\pm 10$  mm) and on the picking of the maximum amplitude ( $\pm 2$  samples around the maximum amplitude).

11 Amplitude ratios of seismoelectric to seismic field as a function of  $S_w$  measured during the imbibition of the third cycle in a) and c), and during the drainage of the third cycle in b) and d) at offset = 0.2 m (blue squares), at offset = 0.3 m (green circles) and offset = 0.4 m (red triangles). The amplitude ratios obtained in the "static approach" are obtained in a) and b) by picking the maximum amplitude in time signals (Time-static), and in c) and d) by picking maximum amplitudes of seismic and seismoelectric first arrival in the C(a,b) map. The low frequency transfer function  $|\psi_{P-1f}(S_w)|$  predictions are obtained by applying an electrokinetic coefficient 2 times smaller compared to the theoretical  $C_{ek}$  computed in Appendix A. They are superimposed in Fig. a) and b) using the model of Jackson (2010) in solid line, Guichet et al. (2003) long dashed line and Revil et al. (2007) short dashed line.

12 Amplitude ratios of seismoelectric to seismic field as a function of  $S_w$  measured during the imbibition (a) and drainage (b) of the third cycle. These data are obtained with the "dynamic approach" by picking the maximum amplitude at the main frequency of seismoelectric data, and, thereafter, by picking the counterpart seismic amplitude at that same seismoelectric main frequency (denoted SEMF, "SeismoElectric Main Frequency") in local maxima curve of the  $C(a, b)$  maps. Dynamic transfer functions are also computed at the observed frequency for each offset, using the Jackson (2010) model with an electrokinetic coefficient 2 times smaller compared to the theoretical  $C_{ek}$  computed in Appendix A.

13 Example of a Continuous Wavelet Transform (CWT) performed on seismic data. a) Mother wavelet function chosen in the present study: Mexican hat wavelet. b) Seismic record  $v_s$  time obtained during the third drainage. The first "lobe" corresponding to the first arrival is highlighted. c) Conversion from scale to frequency using eq. (B6) with  $f_0 = 0.25$  Hz. d)  $C(a, b)$  spectrum map obtained by a CWT of the seismic signal shown in b), the included figure shows the local maxima (black line) extracted to get a local spectrum. Colors indicate the amplitude of  $C(a, b)$  for a given  $a$  and  $b$ .

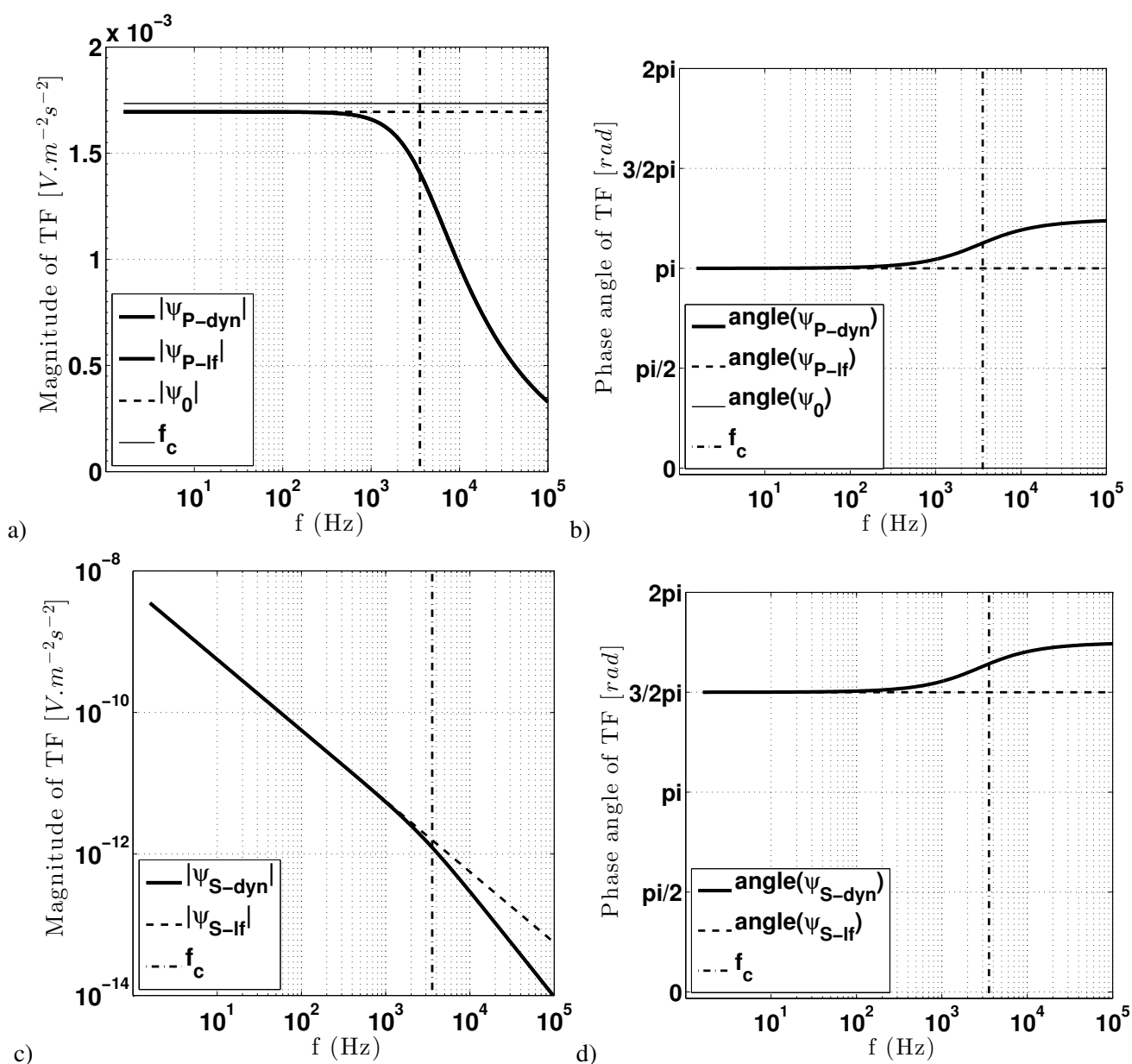


**Figure 1.** Magnitude a) and phase angles b) as a function of the frequency  $f$  respectively for the P-waves dynamic transfer function  $\psi_{P-dyn}$ , for the P-waves low frequency transfer function  $\psi_{P-lf}$  and for the P-waves simplified low frequency transfer function  $\psi_0$  in a saturated sand (formulation in Appendix A and physical parameters in Table 1). c) and d) are the magnitudes and phase angles of the S-waves transfer functions ( $\psi_{S-dyn}$  and  $\psi_{S-lf}$ ) for the same parameters of the computations shown in a) and b). The Biot's frequency  $f_c$  is shown with a vertical dashed line on all graphs.

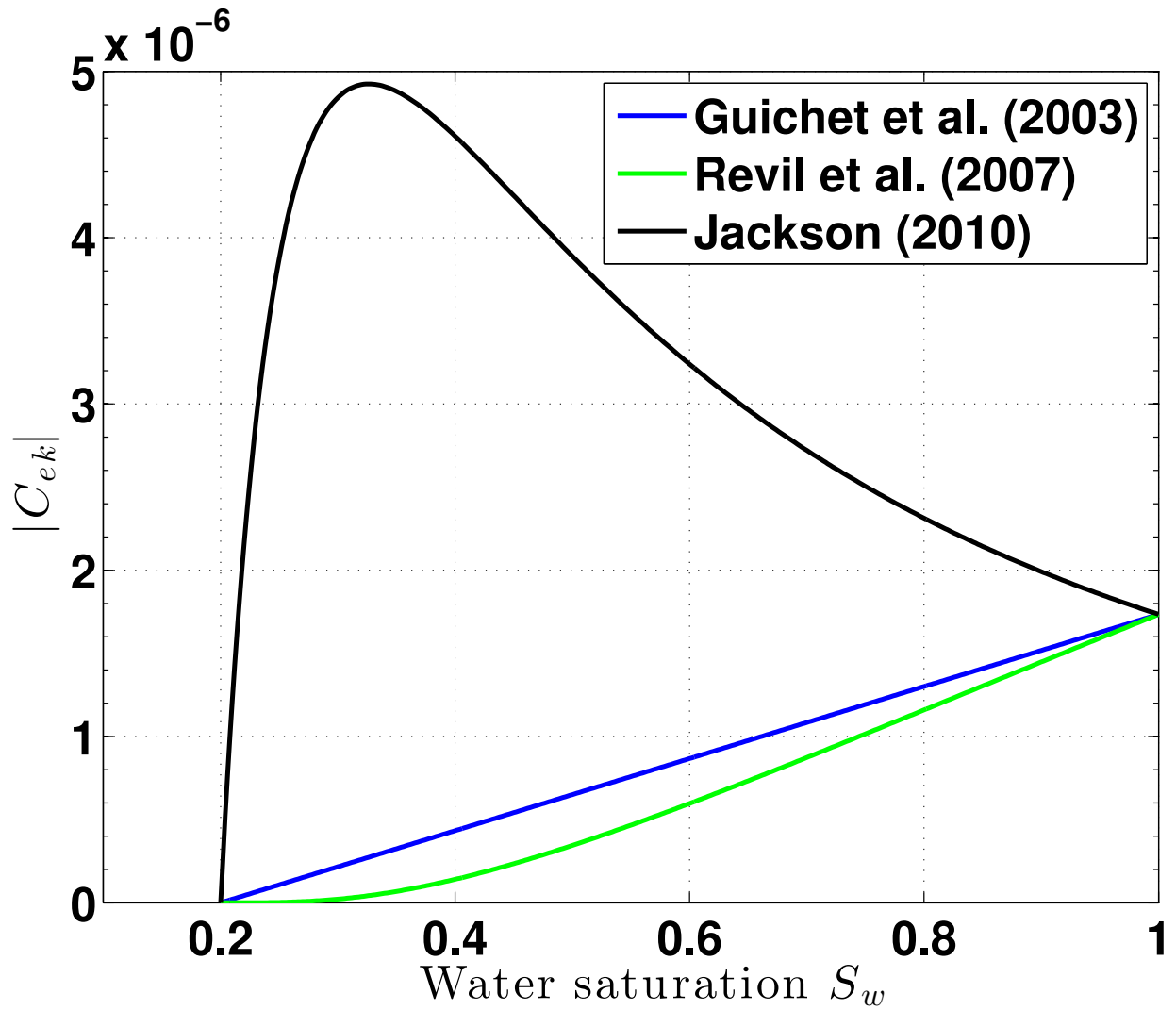


**Figure 2.** Absolute values of the coupling electrokinetic coefficients  $|C_{ek}(S_w)|$  as a function of the water saturation  $S_w$ , for different electrokinetic models. The analytical formulations of the models are shown explicitly in Appendix B.



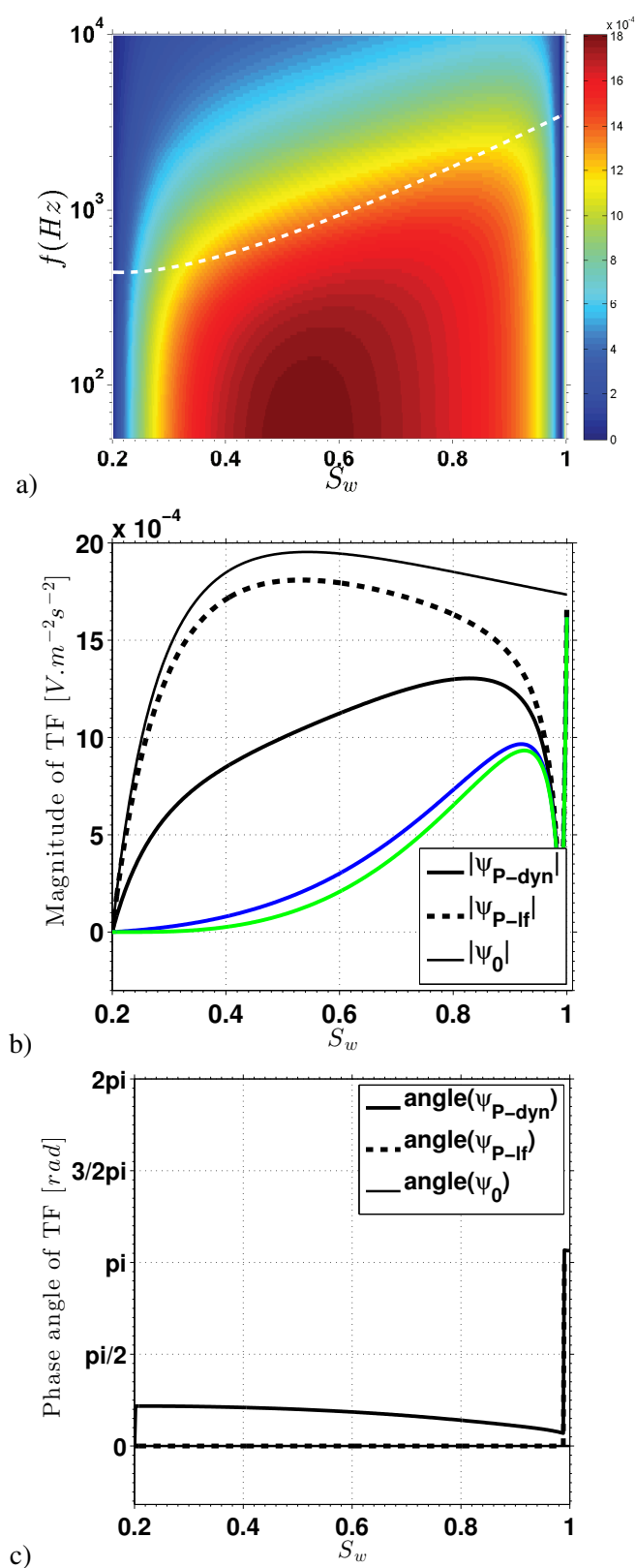


**Figure 3.** a) Magnitude of the P-waves dynamic transfer function  $|\psi_{P-dyn}(S_w, \omega)|$  as a function of frequency  $f$  and saturation  $S_w$ , based on the Jackson (2010) model for electrokinetic coupling. The white line gives Biot's frequency values as a function of  $S_w$ . b) and c): Magnitudes and phase angles as a function of the saturation  $S_w$  respectively for the P-waves dynamic transfer function  $\psi_{P-dyn}$  at  $f = 1.5$  kHz, for the P-waves low frequency transfer function  $\psi_{P-lf}$  and for the P-waves simplified low frequency transfer function  $\psi_0$  in a partially saturated silica sand. *Magnitude of dynamic transfer functions obtained with the models of Guichet et al. (2003) and Revil et al. (2007) are respectively displayed by blue and green curves.*

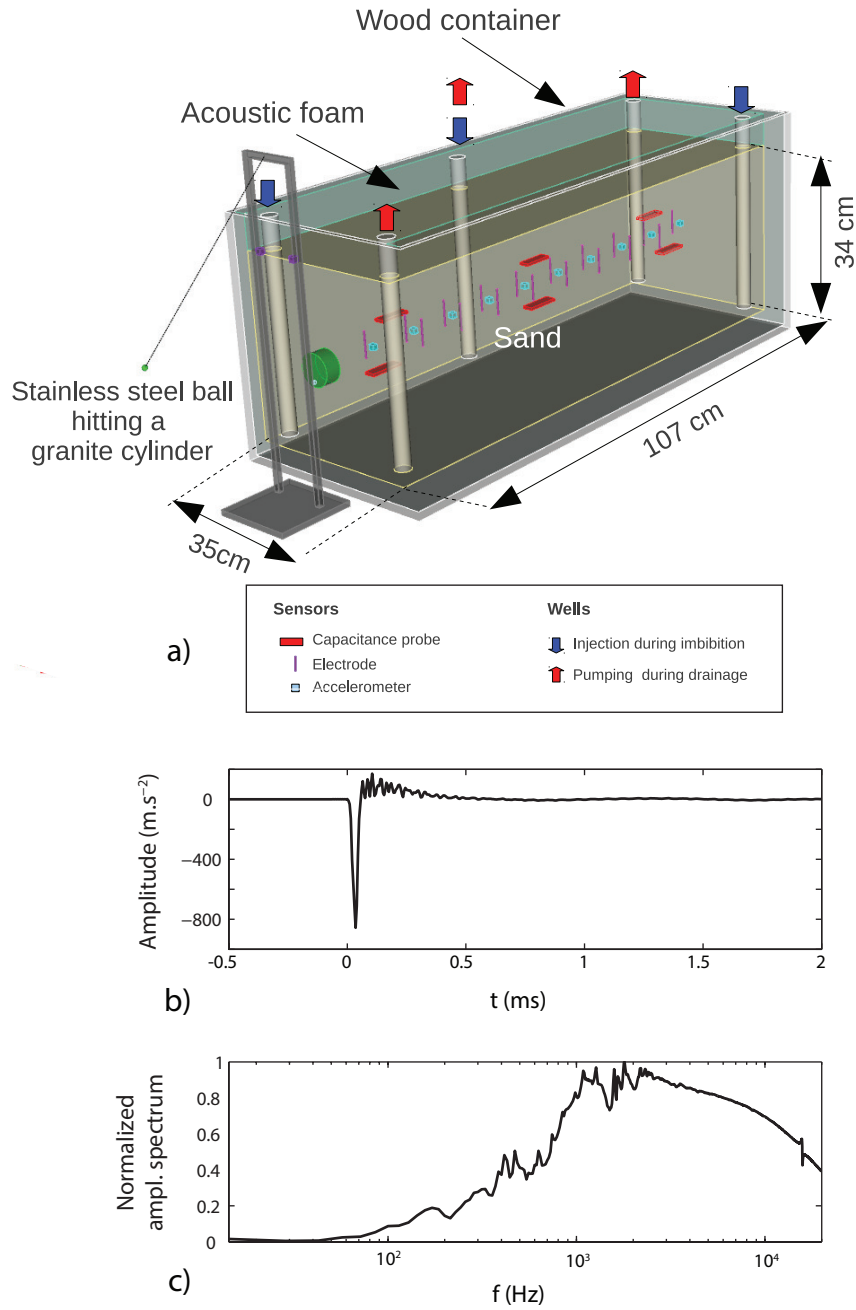


**Figure 4.** a) Sketch of the experimental apparatus used in the present study. b) Typical record of the seismic source signal (steel ball hitting the granite) *vs* time, recorded by an accelerometer located on the granite cylinder. c) Normalized amplitude spectrum of the source signal shown in b) as a function of frequency.

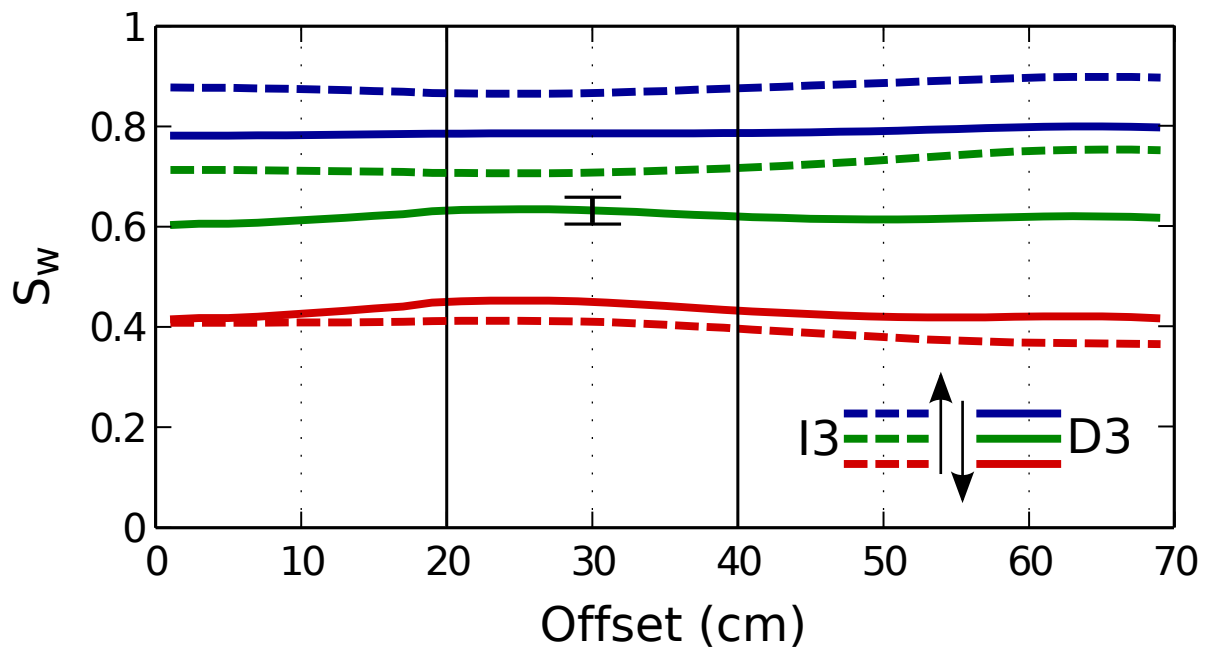


**Figure 5.** Example of water saturation measurements along the receivers array for different values of  $S_w$ . Variations of  $S_w$  between offset=0.2m and 0.4m are lower than uncertainties on  $S_w$  measurements displayed as an example at offset=0.3m, during D3, when  $S_w$  is close to 0.6.

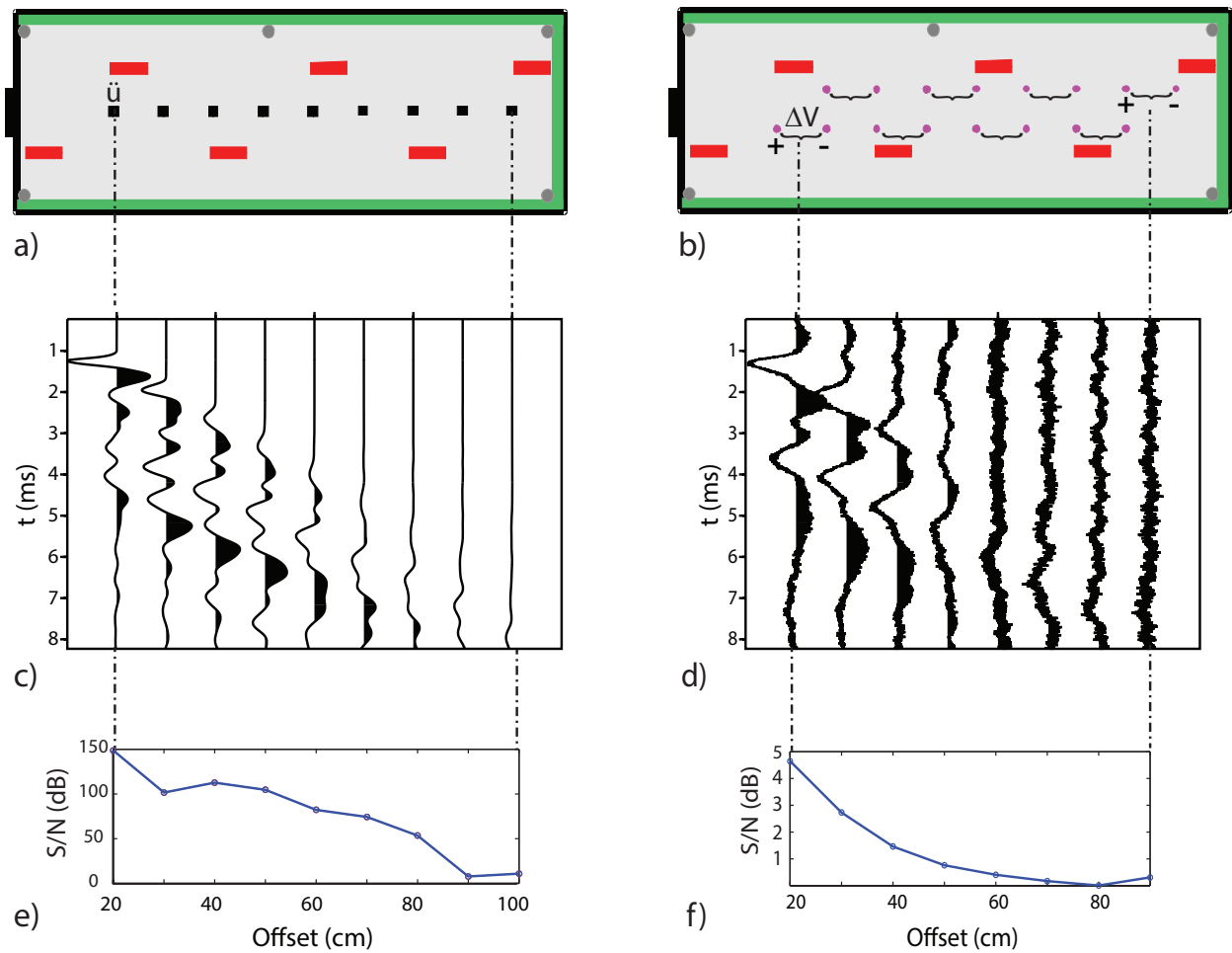


**Figure 6.** a) View from above of the horizontal plane of the experimental set-up containing accelerometers (black squares) and capacitance probes (red rectangles). b) View from above of the same horizontal plane shown in a) containing dipoles (couple of electrodes in magenta). c) Seismic records at various offsets (source/receiver distance) obtained at the beginning of the drainage of the third cycle for  $S_w \approx 0.9$ . d) Seismoelectric record at various offsets recorded simultaneously to the seismic data shown in c). e) Signal to noise ratio of the data shown in c) *vs* offsets. f) Signal to noise ratio of the data shown in d) *vs* offsets.

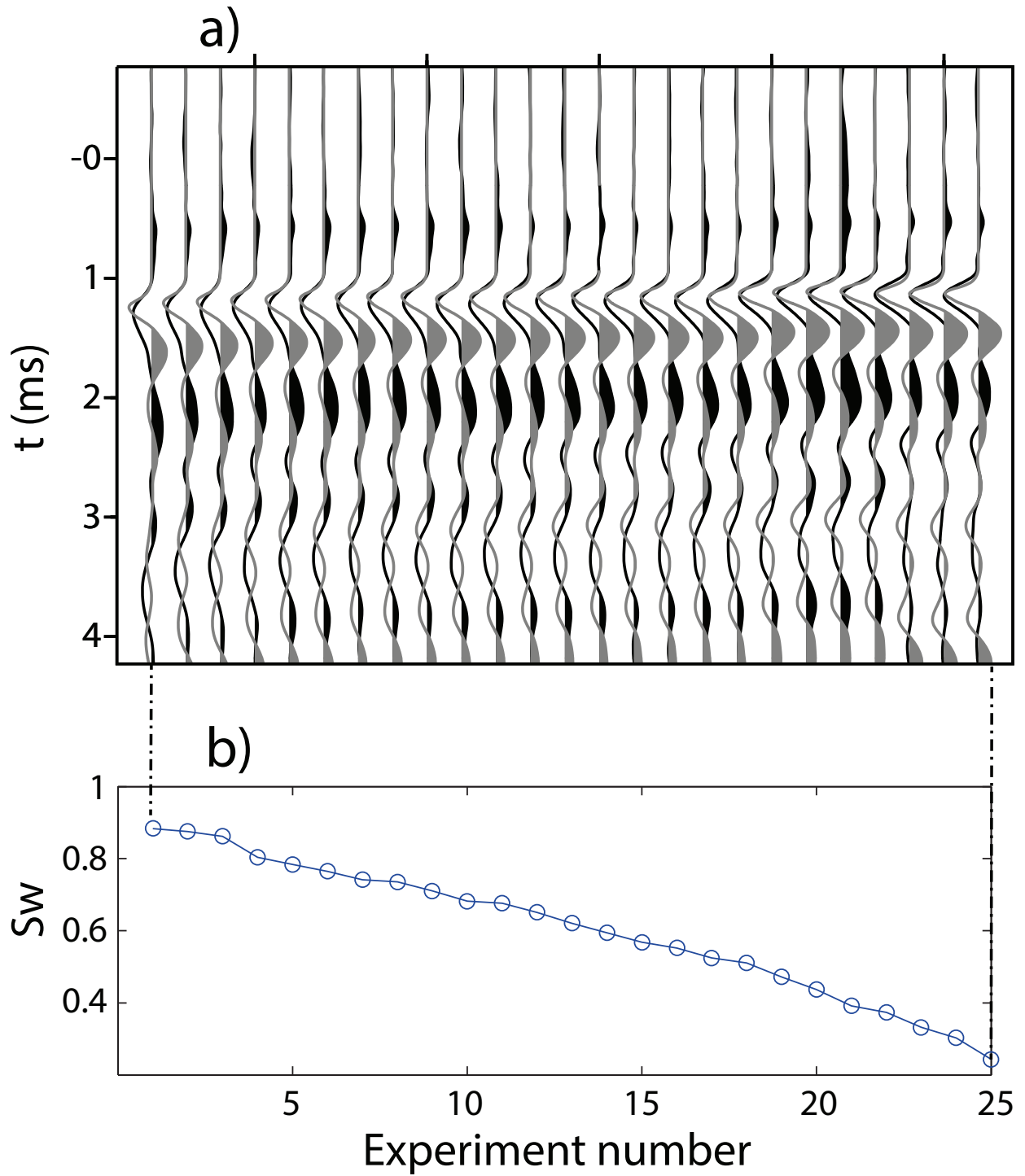


**Figure 7.** a) Normalised seismic traces (grey) and seismoelectric fields (black) measured at offset = 0.2 m during the third drainage. b)  $S_w$  coefficient as a function of the experiment number shown in a).

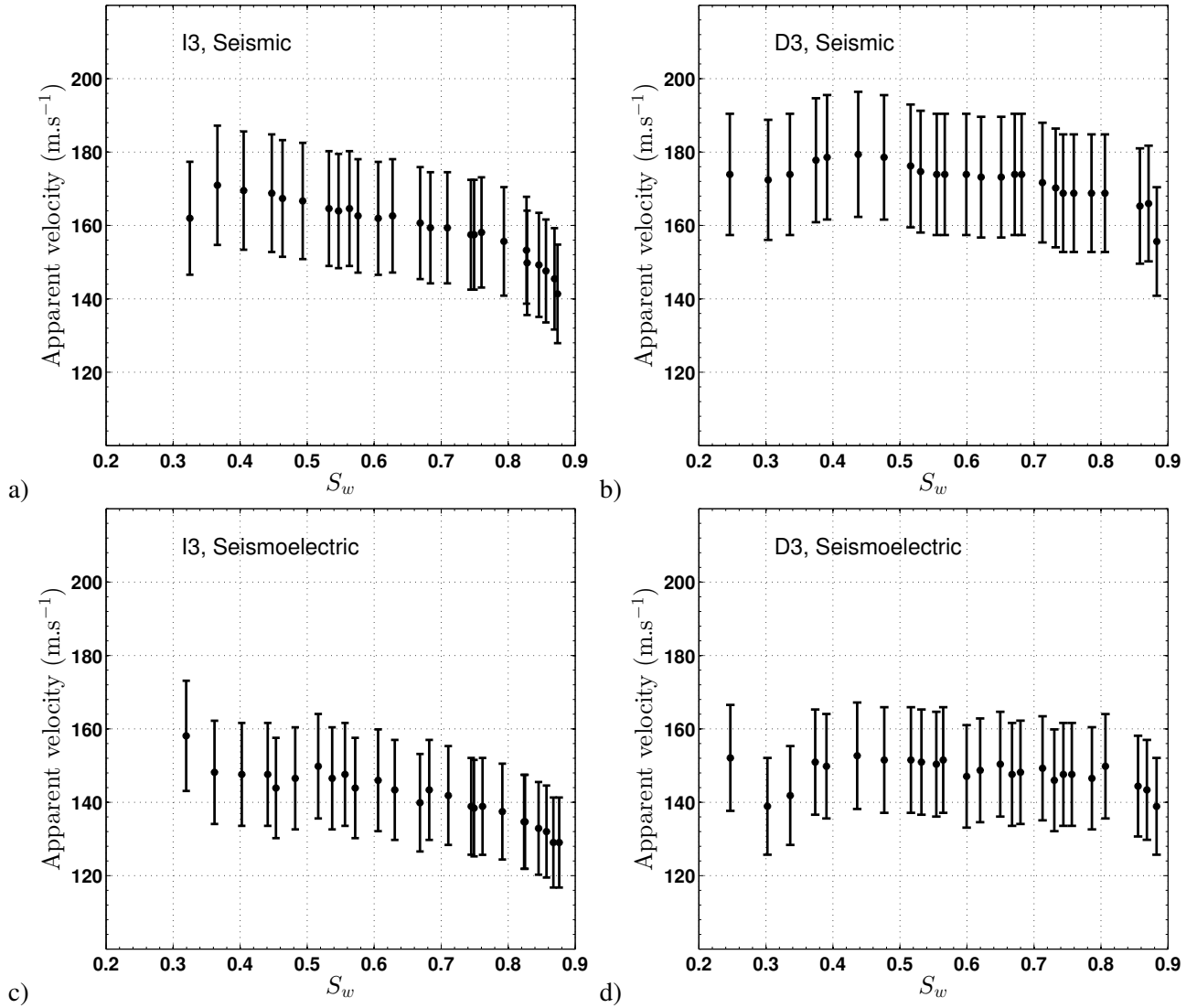


**Figure 8.** Apparent seismic and seismoelectric velocities measured during the third cycle as a function of  $S_w$ . a), b), c) and d) are respectively the seismic velocities during imbibition (I3), seismic velocities during drainage (D3), seismoelectric velocities during imbibition and seismoelectric velocities during drainage. The error bars, around 10% of the measured velocity, originate from uncertainties on the accelerometers locations ( $\pm 5$  mm), on the picking times ( $\pm 4 \times 10^{-5}$  s) and on the dipole lengths between coupled electrodes ( $\pm 10$  mm).

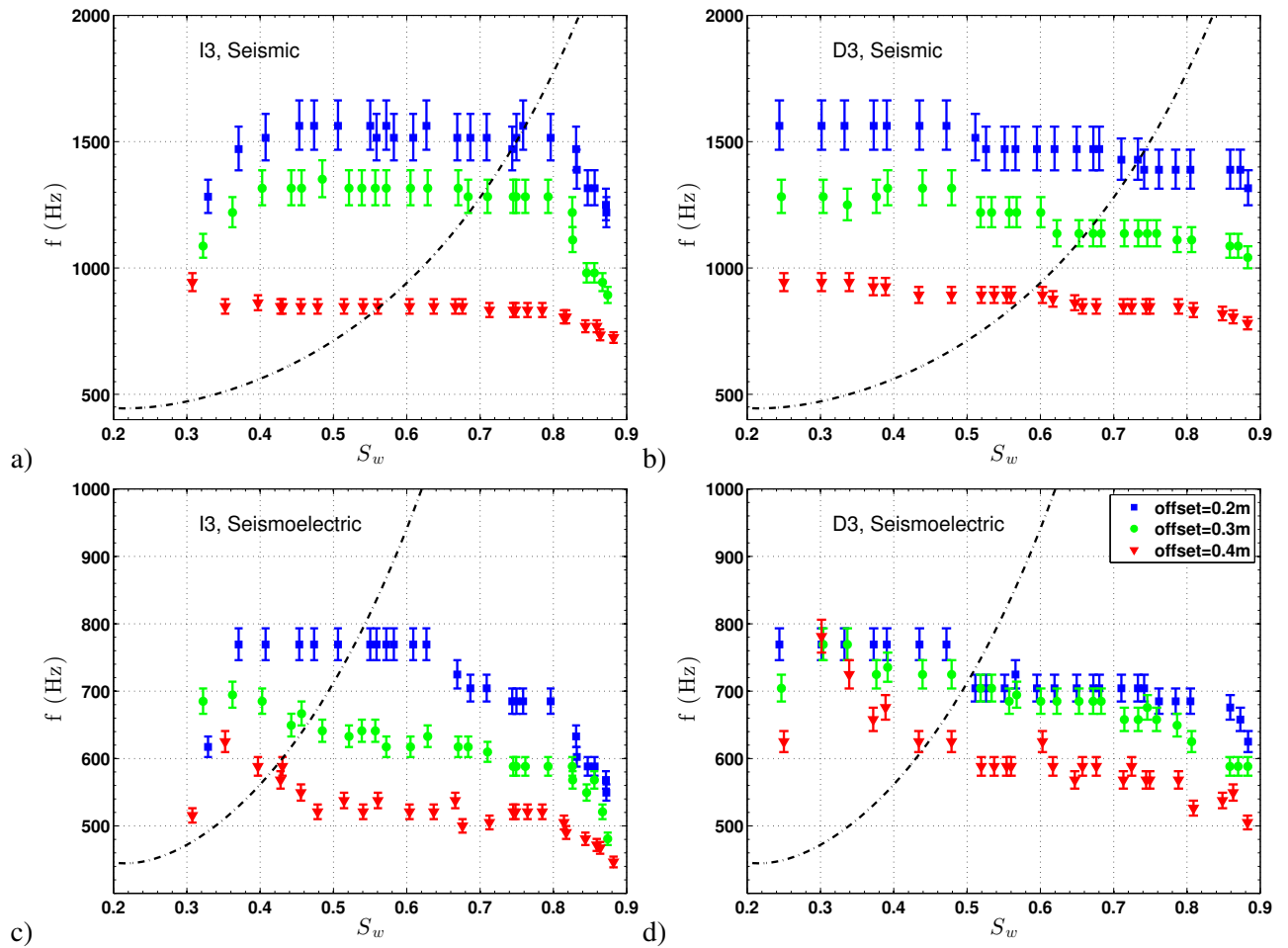


**Figure 9.** Main frequency (picked from a CWT signal processing) obtained during the third cycle from respectively a) the seismic data during imbibition, b) the seismic data during drainage, c) the seismoelectric data during imbibition and d) seismoelectric data during drainage. All figures are shown as a function of the saturation  $S_w$  and for three different offsets: blue squares 0.2 m, green circles 0.3 m and red triangles 0.4 m. The error bars originate from uncertainties in picking pseudo frequencies ( $\pm 2$  samples around the maximum amplitude). The variations in Biot's frequency *vs* saturation (computed from eq. (5) and Appendix A) during those experiments are shown with a dashed black line.

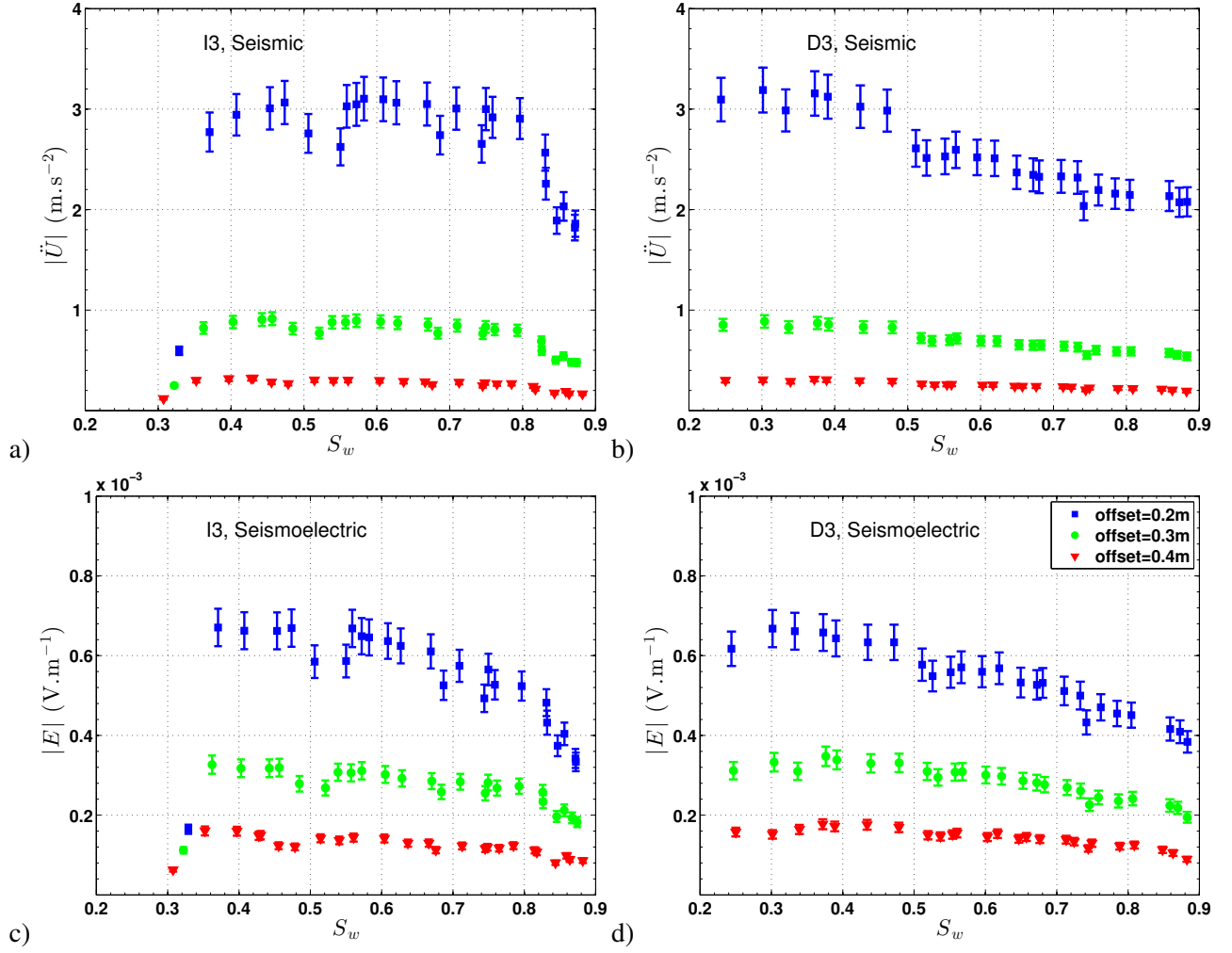


**Figure 10.** First arrival amplitude (picked in time signals) during the third cycle from respectively a) the seismic data during imbibition, b) the seismic data during drainage, c) the seismoelectric data during imbibition and d) seismoelectric data during drainage. All figures are shown as a function of the saturation  $S_w$  and for three different offsets: blue squares 0.2 m, green circles 0.3 m and red triangles 0.4 m. The associated error bars (around 7%) in seismic and seismoelectric amplitudes originate from uncertainties in the receivers location ( $\pm 5$  mm), in the dipole length ( $\pm 10$  mm) and on the picking of the maximum amplitude ( $\pm 2$  samples around the maximum amplitude).



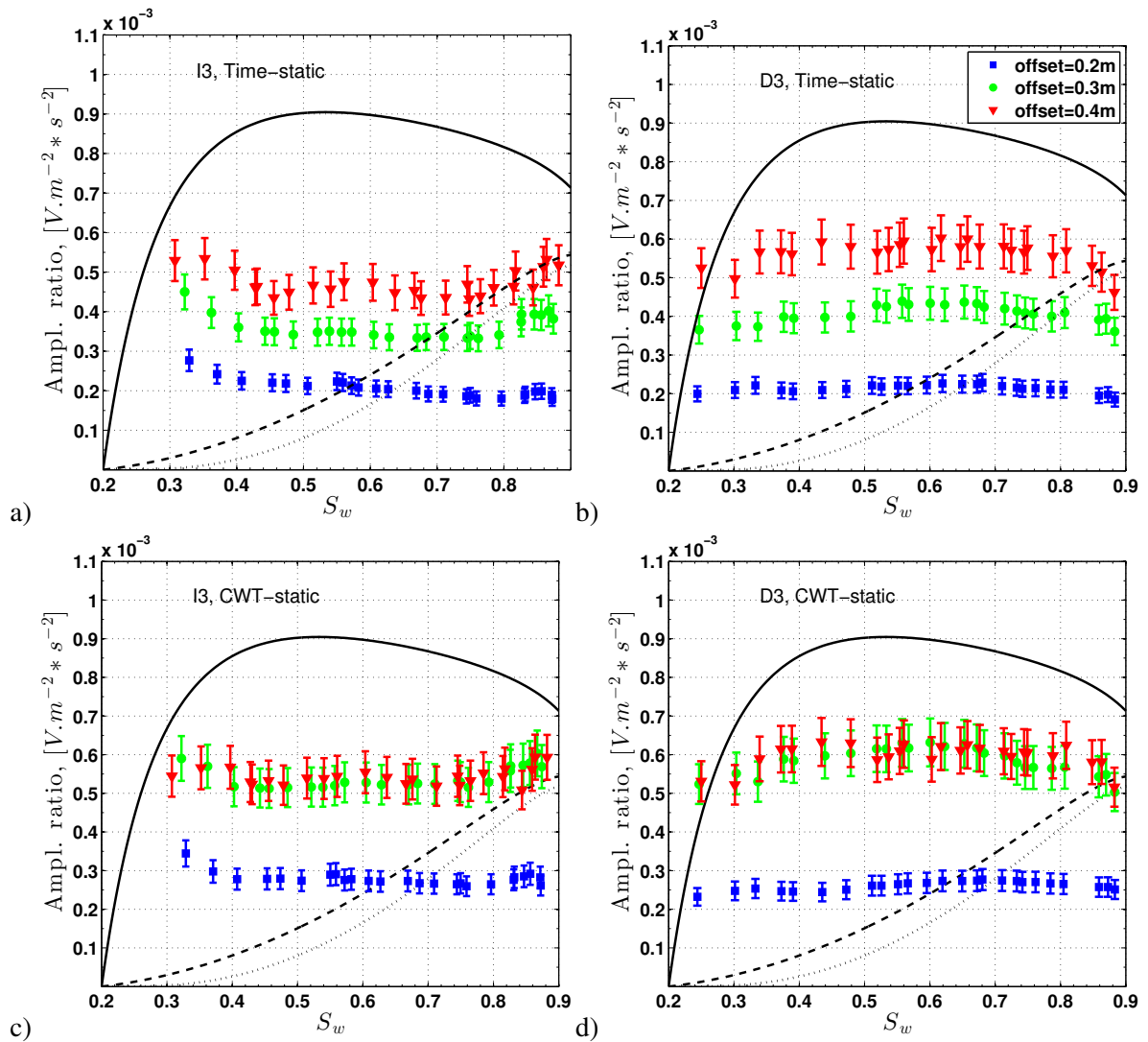


**Figure 11.** Amplitude ratios of seismoelectric to seismic field as a function of  $S_w$  measured during the imbibition of the third cycle in a) and c), and during the drainage of the third cycle in b) and d) at offset = 0.2 m (blue squares), at offset = 0.3 m (green circles) and offset = 0.4 m (red triangles). The amplitude ratios obtained in the "static approach" are obtained in a) and b) by picking the maximum amplitude in time signals in the C(a,b) map. The low frequency transfer function  $|\psi_{P-If}(S_w)|$  predictions are obtained by applying an electrokinetic coefficient 2 times smaller compared to the theoretical  $C_{ek}$  computed in Appendix A. They are superimposed in Fig. a) and b) using the model of Jackson (2010) in solid line, Guichet et al. (2003) long dashed line and Revil et al. (2007) short dashed line.

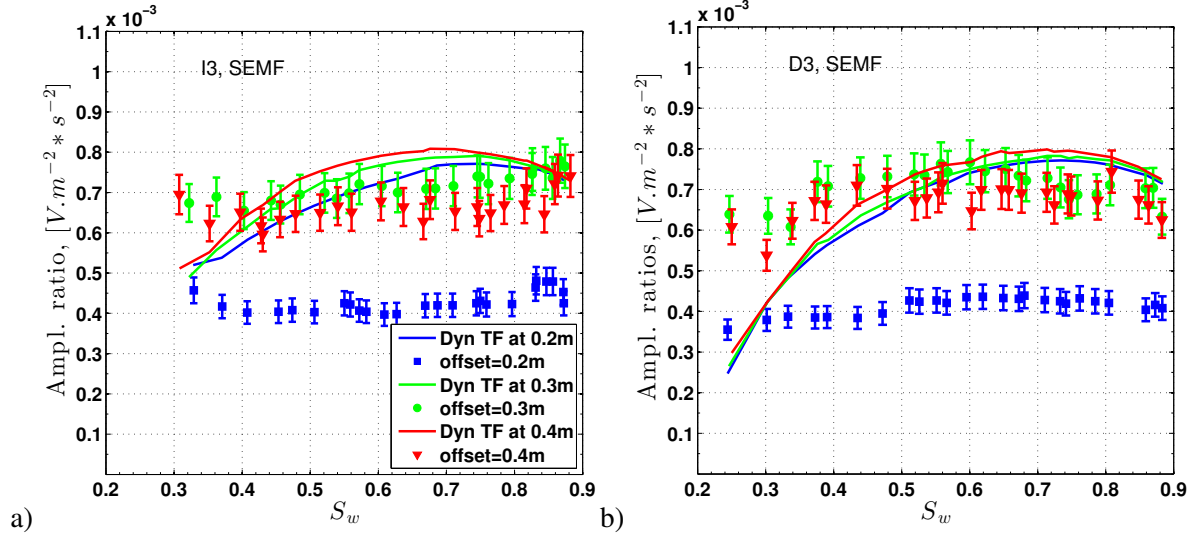


**Figure 12.** Amplitude ratios of seismoelectric to seismic field as a function of  $S_w$  measured during the imbibition (a) and drainage (b) of the third cycle. These data are obtained with the “dynamic approach” by picking the maximum amplitude at the main frequency of seismoelectric data, and, thereafter, by picking the counterpart seismic amplitude at that same seismoelectric main frequency (denoted SEMF, “SeismoElectric Main Frequency”) in local maxima curve of the  $C(a, b)$  maps. Dynamic transfer functions are also computed at the observed frequency for each offset, using the Jackson (2010) model with an electrokinetic coefficient 2 times smaller compared to the theoretical  $C_{ek}$  computed in Appendix A.

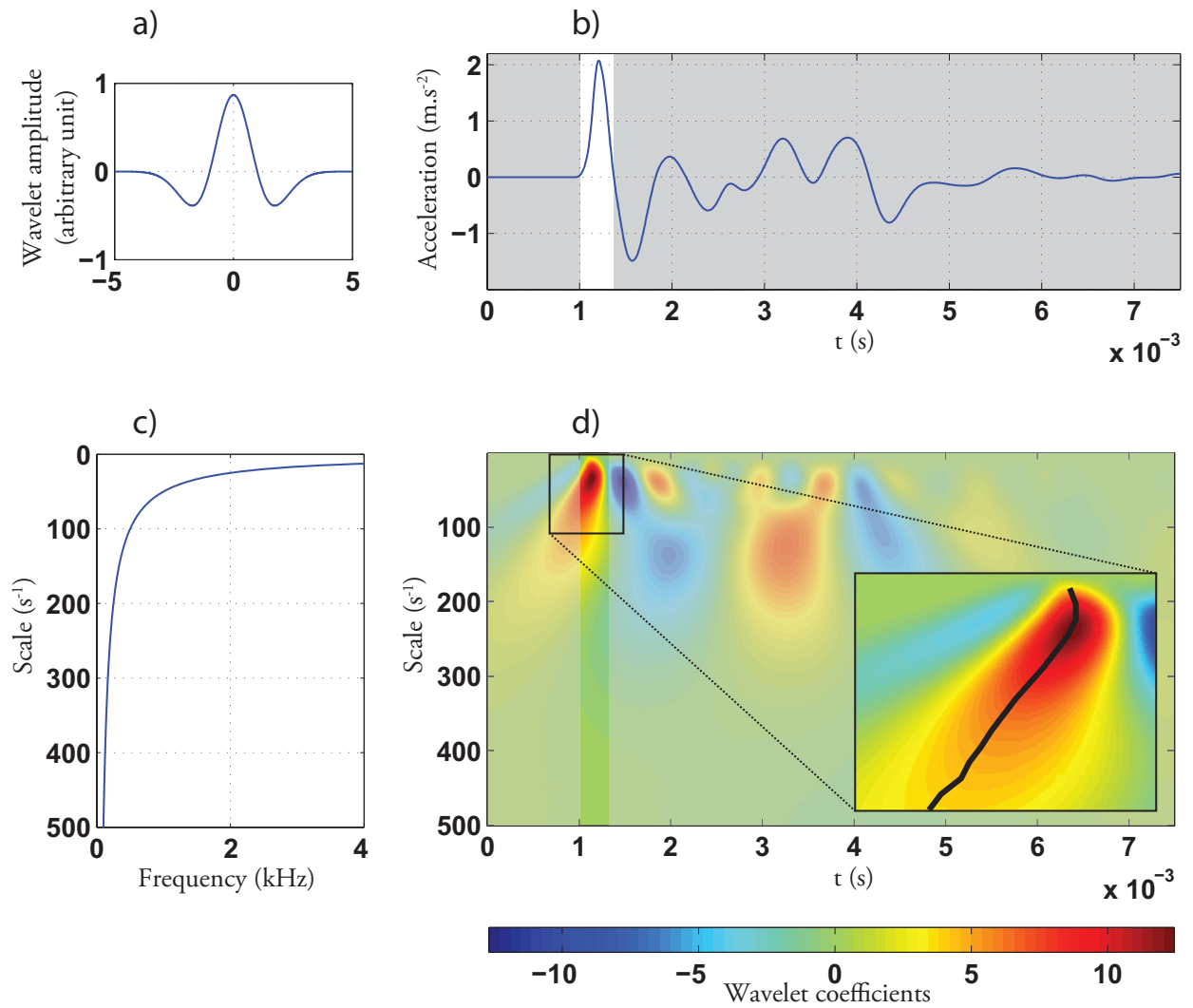


**Figure 13.** Example of a Continuous Wavelet Transform (CWT) performed on seismic data. a) Mother wavelet function chosen in the present study: Mexican hat wavelet. b) Seismic record  $vs$  time obtained during the third drainage. The first “lobe” corresponding to the first arrival is highlighted. c) Conversion from scale to frequency using eq. (B6) with  $f_0 = 0.25$  Hz. d)  $C(a, b)$  spectrum map obtained by a CWT of the seismic signal shown in b), the included figure shows the local maxima (black line) extracted to get a local spectrum. Colors indicate the amplitude of  $C(a, b)$  for a given  $a$  and  $b$ .

**LIST OF TABLES**

- 1 Definition and values of the physical parameters involved in the computations of the transfer functions in a water saturated silica sand.
- 2 List of the various functions  $f(S_w)$  used in the electrokinetic coefficient depending on saturation  $C_{ek}(S_w) = C_{ek}(S_w = 1)f(S_w)$ . The various used notations are detailed in Appendix B.
- 3 Definition and values of the physical parameters involved in the computations of the transfer functions in a partially saturated silica sand.  $f(S_w)$ , entering in the definition of  $C_{ek}(S_w)$ , are given in Table 2.

Physical parameter	Notation	Value	Units	
Fluid				
Density	$\rho_f$	$10^3$	$\text{kg}\cdot\text{m}^{-3}$	
Dynamic viscosity	$\eta_f$	$10^{-3}$	$\text{Pa}\cdot\text{s}$	
Elastic modulus	$K_f$	$2.5\times 10^9$	$\text{Pa}$	
Electrical conductivity	$\sigma_f$	$1.17\times 10^{-2}$	$\text{S}\cdot\text{m}^{-1}$	measured
Solid (silica sand grains)				
Grain density	$\rho_s$	$2.65\times 10^3$	$\text{kg}\cdot\text{m}^{-3}$	
Elastic modulus	$K_s$	$3.6\times 10^{10}$	$\text{Pa}$	
Porous medium				
Porosity	$\phi$	0.4		measured
Intrinsic permeability	$k_0$	$1.02\times 10^{-11}$	$\text{m}^2$	measured
Tortuosity	$\gamma_0$	1.75		from Berryman (1981)
Drained or frame modulus	$K_D$	$2.5\times 10^7$	$\text{Pa}$	from seismic velocities
Shear frame modulus	$G$	$1.54\times 10^7$	$\text{Pa}$	
Pore space term	$m$	6		from Pride (1994)
Electrokinetic coef.	$C_{ek}$	$-1.73\times 10^{-6}$	$\text{V}\cdot\text{Pa}^{-1}$	from Guichet et al. (2003), see Appendix B

**Table 1.** Definition and values of the physical parameters involved in the computations of the transfer functions in a water saturated silica sand.

Model	$f(S_w)$	Reference
Linear model	$S_e$	Guichet et al. (2003)
Volume averaging	$S_e^{\frac{2+3\lambda}{\lambda}} / S_w^{n+1}$	Revil et al. (2007)
Capillary tubes	$S_e / S_w^n$	Jackson (2010)

**Table 2.** List of the various functions  $f(S_w)$  used in the electrokinetic coefficient depending on saturation  $C_{ek}(S_w) = C_{ek}(S_w = 1)f(S_w)$ . The various used notations are detailed in Appendix B.

Physical parameter	Notation	Value	Units	
Fluid (water and gas)				
Density	$\rho_w$	$10^3$	$\text{kg}\cdot\text{m}^{-3}$	
Dynamic viscosity	$\eta_w$	$10^{-3}$	$\text{Pa}\cdot\text{s}$	
Elastic modulus	$K_w$	$2.5 \times 10^9$	$\text{Pa}$	
Electrical conductivity	$\sigma_w$	$1.17 \times 10^{-2}$	$\text{S}\cdot\text{m}^{-1}$	measured
Gas density	$\rho_g$	1.2	$\text{kg}\cdot\text{m}^{-3}$	
Dynamic viscosity	$\eta_g$	$10^{-5}$	$\text{Pa}\cdot\text{s}$	
Elastic modulus of air	$K_g$	$1.5 \times 10^5$	$\text{Pa}$	
Solid (silica sand grains)				
Grain density	$\rho_s$	$2.65 \times 10^3$	$\text{kg}\cdot\text{m}^{-3}$	
Elastic modulus	$K_s$	$3.6 \times 10^{10}$	$\text{Pa}$	
Porous medium				
Porosity	$\phi$	0.4		measured
Intrinsic permeability	$k_0$	$1.02 \times 10^{-11}$	$\text{m}^2$	measured
Tortuosity	$\gamma_0$	1.75		from Berryman (1981)
Drained or frame modulus	$K_D$	$2.5 \times 10^7$	$\text{Pa}$	from Walton (1987), checked on s
Shear frame modulus	$G$	$1.54 \times 10^7$	$\text{Pa}$	
Electrokinetic coef.	$C_{ek}(S_w)$	$-1.73 \times 10^{-6} \times f(S_w)$	$\text{V}\cdot\text{Pa}^{-1}$	from Guichet et al. (2003), see Appendix B
Residual water saturation	$S_{w0}$	0.2		
Pore space term	$m$	6		from Pride (1994)
Second exponent of Archie's law	$n$	2.58		from Doussan & Ruy (2009)
Curve shape parameter	$\lambda$	1.7		from Revil et al. (2007)

**Table 3.** Definition and values of the physical parameters involved in the computations of the transfer functions in a partially saturated silica sand.  $f(S_w)$ , entering in the definition of  $C_{ek}(S_w)$ , are given in Table 2.